KRONOS FUSION ENERGY

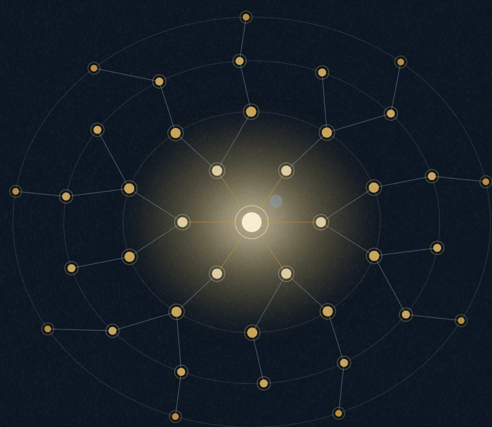

PAPER 2.75 · THE KRONOS 2026 SERIES

A Real-Time Control Suite for a Compact Negative-Triangularity Spherical-Tokamak Breeder: Profile, Shape, Vertical-Stability, q-Profile, and Solenoid-Free Ramp Controllers

A compact, high-current spherical tokamak leaves little time to react and no room for an uncontrolled excursion, so its controllers must be simultaneously fast, coordinated, and...

Read it live — 3-D model · physics validator · film series

BY P I FORD

2026 · EDITORIAL EDITION

THE OFFICIAL RECORD

What this document is, and how to read its numbers

This is a combined editorial. It gathers, in one volume, the two design studies Kronos Fusion Energy released in 2026 — a compact spherical-tokamak tritium/helium-3 breeder and a deuterium–helium-3 tandem-mirror generator — together with the intellectual-property estate, the people, and, in the internal edition, the full commercial case. The scientific text is the same text that appears in the arXiv preprints and the journal submissions; the editorial adds the apparatus a reader needs to hold the whole program at once, and nothing in the physics is altered to fit it.

THE HONESTY STANCE IS THE ASSET

Every headline quantity carries an **evidence class** — DERIVED RECOMPUTED MEASURED REQUIREMENT — and, where a number is a modelled extrapolation rather than a demonstrated value, it is labelled as such and its downside is shown next to it. Several quantities in the underlying corpus moved after first publication; where a value has been withdrawn or restated, the record says so plainly. This is deliberate: a diligence team will find the load-bearing assumptions, so the document surfaces them first.

TWO EDITIONS

This volume is issued in two editions. The **public edition** (light) carries the physics and the design only — no dollar, price, or per-kilogram figure appears anywhere in it. The **internal edition** (dark) adds the economics, the funding architecture, and the defense-commercial analysis, and is marked *Confidential* accordingly; it is not for public distribution. Where the commercial case rests on a modelled assumption rather than a demonstrated one, it is labelled as such and its downside is shown alongside it, on the same terms as the physics.

TITLE	The Kronos Fleet — Hyperion · Aegis · MetroVolt: A Combined Design & Commercialization Study
AUTHOR	Priyanca Ford, Founder & CEO, on behalf of Kronos Fusion Energy
EDITION	2026 Combined Editorial · first issue
COMPANION WORKS	The five-paper arXiv drop — (1) Breeder, (2) Burner, (3) REBCO magnet & tape, (4) Direct Energy Conversion, (5) AI/ML/Quantum control — with matching numbered Zenodo deposits, plus the IOP journal and IAEA-FEC submissions. Patents were filed before the drop.
NAMING	Hyperion = the breeder; Aegis (defense) and MetroVolt (data-center) = one generator in two housings. Internal mode letters (D1, L) do not appear on public surfaces.
STATUS	Conceptual design & simulation study. Nothing herein is a construction commitment.

HOW TO READ THIS VOLUME

The fleet at a glance, and the way its numbers are marked

This volume opens with *Orientation*, presents the five research papers as a bound sequence, and closes with the *Apparatus*. *Foundations* sets out the three general results both machines rest on. *Paper One* is the Hyperion breeder; *Paper Two* the Aegis / MetroVolt generator; *Papers Three, Four and Five* are the enabling science — high-field REBCO magnets and tape, direct energy conversion, and the AI / ML / quantum control stack. A *Digital Twin & 3-D Model* part follows, then the *Environmental* profile. The *Economics* and levelized cost and the *Business Case* and diligence record appear in the internal edition only; the *Simulations* proof record and the Apparatus — patent portfolio, team, limitations, and sources — close both editions.

THE FLEET AT A GLANCE

	HYPERION	AEGIS	METROVOLT
Role	Strategic-isotope foundry	Defense installation power	Campus power
Machine	**Spherical tokamak**	**Tandem mirror**	**Tandem mirror**
Fuel	Deuterium–tritium	Deuterium–helium-3	Deuterium–helium-3
Delivers	Tritium · ^{3}He · 14 MeV n	Resilient installation power	Firm campus power
Physics bar	**Fusion gain only**	Closure (gates named)	Closure + lunar ^{3}He
In the fleet	Breeds the fuel	Proves the generator	Commercial destination

HOW THE NUMBERS ARE MARKED

Every headline quantity carries an evidence class — DERIVED from first principles, RECOMPUTED from raw data, MEASURED in hardware, or a REQUIREMENT yet to be met. Financial figures carry a case label and are confined to the internal (confidential) edition. Values that moved after first publication are shown as withdrawn or restated rather than quietly changed. A capability you can evaluate is one whose limits are on the page.

ABSTRACT

A Real-Time Control Suite for a Compact Negative-Triangularity Spherical-Tokamak Breeder: Profile, Shape, Vertical-Stability, q-Profile, and Solenoid-Free Ramp Controllers

A compact, high-current spherical tokamak leaves little time to react and no room for an uncontrolled excursion, so its controllers must be simultaneously fast, coordinated, and provably safe. We present the real-time control suite for the Hyperion breeder (design point $I_p = 9.66\,MA$, $Q = 3.076$, $P_{\text{fus}} = 85.04\,MW$, negative triangularity $\delta = -0.30$, on-axis field $B_0 = 8\,T$, elongation $\kappa = 2.0$, major radius $R_0 = 1.20\,m$, aspect ratio $A = 2.5$, centrepost peak field $16.84\,T$): a family of seventeen closed-loop controllers spanning core profile, plasma shape, vertical stability, q-profile and solenoid-free current ramp-up, unified beneath a single certified safety layer. We write the plant as a control-affine coupling of the Grad–Shafranov equilibrium, the poloidal-flux (current) diffusion equation, a flux-driven transport closure and the axisymmetric conductor circuit, and we cast each control objective as an explicit tracking-or-constraint problem; the safety layer is a control-barrier-function (CBF) quadratic program that projects any commanded action onto the nearest action keeping the closed loop inside the certified safe set $\{\beta_N \leq 3.5\}$. The safety layer is reduced to practice and demonstrated in closed loop: it holds the peak normalized pressure at the boundary ($\beta_N = 3.500$) with **zero violations in 100 episodes**, against a peak $\beta_N = 4.200$ and **50 violations** for the unclamped policy, with the barrier value $h \geq 0$ throughout (forward invariance) and a bounded multiplicative command $u \in [1.06, 1.25]$; in an injected-fault stress test the same clamp caught 3000 of 3000 unsafe actions with zero escapes over 150 000 control steps. Each controller holds a reproduced anchor: a free-boundary shape at $\delta = -0.334$, $q_{95} = 2.90$ and internal inductance $\ell_i = 1.40$; a flux-driven profile with $\tau_E = 0.410$ ($H_{98} \approx 0.94$); a q-profile that is Mercier- and ballooning-stable on every surface with $q > 1$ (the binding external-kink margin is 1.15–$1.31\times$); and a solenoid-free ramp to the $9.66\,MA$ flat-top. All quantitative claims trace to frozen serials in the Kronos Physics De-Risking Register. The result is a coherent, physics-anchored control suite whose safety guarantee is already demonstrated and whose remaining controllers are built to that same certified pattern, with an explicit maturity-gated path to full authority.

Open-access deposit (code & data, CC BY 4.0): DOI 10.5281/zenodo.22645809 · Zenodo community *kronos_fusion_energy*. Explore it live: interactive 3-D model · physics validator.

Keywords: real-time control · control barrier function · model-predictive control · vertical stability · q-profile control · solenoid-free ramp · negative triangularity · spherical-tokamak breeder

CONTENTS

Table of Contents

NOMENCLATURE

Symbols, units, and the names of things

Q	plasma (fusion) gain, P_{fus}/P_{aux}
Q_E	engineering gain, net electric out / recirculating in
H_{98}	confinement enhancement over the IPB98(y,2) scaling
Z_{eff}	effective ion charge
c_{ee}	electron–electron bremsstrahlung leading coefficient, 2.120022 (exact)
τ_E	energy confinement time
I_p	plasma current
R_0, a	major radius, minor radius
κ, δ	elongation, triangularity
β_N	normalized plasma beta (Troyon-normalized)
TBR	tritium breeding ratio
DEC	direct energy conversion
CF	plant capacity factor (availability)
FOAK / NOAK / BOAK	first / n^{th} / best of a kind
Hyperion	the ST breeder (internal: Mode D2)
Aegis	the generator, defense/installation housing (internal: Mode M)
MetroVolt	the generator, data-center housing (Mode M)

real-time control; control barrier function; model-predictive control; vertical stability; q-profile control; solenoid-free ramp; negative triangularity; spherical-tokamak breeder

§ 1

Introduction

CONTROLLING A COMPACT, HIGH-CURRENT SPHERICAL TOKAMAK

A spherical tokamak (ST) confines a large plasma current in a small volume, which is exactly what makes it an attractive compact neutron source and breeder platform [1,2] and, at the same time, what makes it demanding to control. The Hyperion breeder holds $I_p = 9.66\,MA$ at a major radius of only $R_0 = 1.20\,m$ behind a centrepost magnet at a peak field of $16.84\,T$, in a negative-triangularity ($\delta = -0.30$) regime. In a device this compact and this highly loaded the characteristic times of vertical instability, of the fastest magnetohydrodynamic (MHD) modes, and of thermal transients are short, and — because it is a nuclear system — every actuation carries a safety consequence. Autonomy is therefore not a convenience but a design requirement: the controller must track demanding setpoints across the pulse and, above all, must never cross a stability or engineering limit. This paper presents the breeder control suite that meets both demands: a family of real-time controllers organized by physical function, each anchored to a reproduced design result, and topped by a certified safety layer that is demonstrated end-to-end.

THE STATE OF TOKAMAK CONTROL

Feedback control of tokamak equilibria and profiles is a mature discipline. Magnetic diagnostics feed real-time equilibrium reconstruction [5]; shape and vertical-position controllers close the loop on the poloidal-field (PF) coil currents [6,7]; and physics-based profile simulators such as RAPTOR now run inside the control cycle to predict and steer the current-density profile in real time [8,9]. More recently, learned controllers have entered the loop: Degrave *et al.* trained a deep reinforcement-learning agent to command the TCV coil voltages and produce a variety of plasma shapes — including negative triangularity — directly from magnetic measurements [10]; Seo *et al.* showed a reinforcement-learning policy that actively avoids the tearing instability [11]; and deep networks forecast disruptive instabilities across machines [12]. In parallel, the safe-control community has made formal safety enforceable at run time through control-barrier functions (CBFs), which render a designated safe set forward-invariant by a minimally-invasive quadratic-program (QP) projection of the nominal action [13,14], and through constrained model-predictive control (MPC), which optimizes actuation over a receding horizon subject to hard constraints [15,16]. These two threads — fast, physics-faithful plasma models and provable run-time safety — are the raw material of an autonomous fusion controller; what has been missing for a compact nuclear ST is a single suite that binds them together, controller by controller, against a frozen physics baseline.

THE NEGATIVE-TRIANGULARITY OPERATING POINT AS A CONTROL TARGET

Negative triangularity is chosen for Hyperion because it accesses good core confinement without the edge pressure pedestal and the associated edge-localized-mode (ELM) cycle of conventional H-mode [3,4]; the corresponding quiet, ELM-free edge is an operational asset — but only if the controller can actively hold the plasma inside the narrow window that keeps it quiet. Two-code gyrokinetic study of this operating point confirms the turbulence suppression that makes the quiescent core an asset [33], and its free-boundary equilibrium and ideal-MHD margins are established separately [34]. The control target is therefore not a generic tokamak but a specific, reproduced design point: $\delta = -0.30$, $\kappa = 2.0$, $q_{95} = 2.90$, $\ell_i = 1.40$, at $I_p = 9.66\,MA$ and $Q = 3.076$. Each of these is a number the suite is built to hold.

CONTRIBUTION

This paper contributes the breeder's real-time control suite as a single, physics-anchored, safety-certified system. Specifically: (i) we write the plant as a control-affine coupling of the Grad–Shafranov equilibrium, the poloidal-flux diffusion (current) equation, a flux-driven transport closure and the axisymmetric conductor circuit (§2); (ii) we cast the five core control objectives — profile, shape, vertical stability, q-profile and solenoid-free ramp — as explicit tracking-or-constraint problems, and derive the CBF safety projection and the receding-horizon controller that acts inside it (§2); (iii) we describe the NVIDIA GPU HPC campaign, naming the codes actually run for this paper and their discretizations, GPU acceleration, problem scale and verification (§3); (iv) we present the seventeen-controller suite with each controller's reproduced anchor and acceptance inequality (§4); (v) we report the demonstrated safety-clamp result and the reproduced physics setpoints (§5); and (vi) we compare quantitatively to the published control literature and give an honest limitation and a maturity-gated path to full authority (§6–§7). Every quantitative claim traces to a frozen entry in the Kronos Physics De-Risking Register [44]; the serial identifiers (e.g. KX-L1-A13, BR-L1-A12) are given inline so each number is auditable.

§ 2

Governing equations and the formal control problem

PLANT MODEL

The controlled plant is the coupling of four sub-models: the magnetic equilibrium, the current (poloidal-flux) diffusion, the energy transport, and the external conductor circuit. We state each and then assemble the control-affine reduced model the controllers act on.

Equilibrium. The axisymmetric magnetic equilibrium is governed by the Grad–Shafranov equation for the poloidal flux $\psi(R, Z)$,

$$\Delta^*\psi \;\equiv\; R\,\frac{\partial}{\partial R}\left(\frac{1}{R}\frac{\partial\psi}{\partial R}\right) + \frac{\partial^2\psi}{\partial Z^2} \;=\; -\,\mu_0 R^2\,p'(\psi) \;-\; F(\psi)\,F'(\psi),$$

with kinetic pressure $p(\psi)$, poloidal-current function $F(\psi) = RB_\phi$, and $(\cdot)' = \mathrm{d}/\mathrm{d}\psi$. The plasma boundary is the outermost closed flux surface; in a free-boundary problem it is set by the balance of the plasma current against the PF and centrepost conductor currents, so that the shape descriptors — elongation κ, triangularity δ, the edge safety factor q_{95} and the internal inductance ℓ_i — are outputs of (1) driven by the coil currents [7]. The reproduced free-boundary solve of the Hyperion design point (serial BR-L1-A12) returns $I_p = 9.66\,MA$, $\beta_p = 0.371$, $\delta = -0.334$, $q_{95} = 2.90$, $\ell_i(3) = 1.40$ and $\beta_N = 2.13$ (figure 4).

Current (poloidal-flux) diffusion. The evolution of the current-density profile — and thus of the q-profile the suite must shape — follows the poloidal-flux diffusion equation on the normalized toroidal-flux coordinate ρ,

$$\sigma_\parallel \frac{\partial\psi}{\partial t} = \frac{1}{\mu_0}\frac{1}{\rho}\frac{\partial}{\partial\rho}\left(\rho\,\frac{\partial\psi}{\partial\rho}\right) - \langle J_{\mathrm{ni}}\cdot B\rangle, \qquad q(\rho) = \frac{\mathrm{d}\Phi}{\mathrm{d}\psi},$$

where $\sigma_\parallel$ is the neoclassical parallel conductivity, J_{ni} the non-inductive current density (bootstrap plus auxiliary current drive), Φ the toroidal flux, and $q(\rho)$ the safety factor. In the solenoid-free ramp there is no central-solenoid loop-voltage source, so the entire flat-top current in (2) must be supplied by bootstrap and auxiliary drive [18,36,37]; this is the defining constraint on the ramp controller.

Transport. The kinetic profiles that enter $p(\psi)$ are set by a flux-driven transport balance. Writing the volume-averaged energy balance for species s,

$$\frac{\partial}{\partial t}\left(\tfrac{3}{2}n_sT_s\right) + \frac{1}{V'}\frac{\partial}{\partial\rho}\left(V'\,q_s\right) = P_{\mathrm{heat},s} - P_{\mathrm{loss},s}, \qquad q_s = -n_s\chi_s\frac{\partial T_s}{\partial\rho} + \tfrac{3}{2}T_s\Gamma_s,$$

with $V'(\rho) = \mathrm{d}V/\mathrm{d}\rho$ the flux-surface volume element, q_s the heat flux, χ_s the turbulent-plus-neoclassical conductivity and Γ_s the particle flux. The turbulent fluxes are the nonlinear gyrokinetic map $q_s = \mathcal{G}(a)$ of the local drive $a = \{R/L_T,\ R/L_n,\ q,\ \hat{s},\ \nu^*, \ldots\}$; we close it with the quasilinear model TGLF [19] inside the flux-matching solver TGYRO [20], itself validated against nonlinear CGYRO [21] at this operating point [33]. The reproduced flux-driven solve (serial BR-L1-A11) returns a confinement time $\tau_E = 0.410$ against a 0.358 reference, an effective $H_{98} \approx 0.94$, with a residual floor of 0.61 that reflects the near-marginal negative-triangularity limit cycle (figure 5).

Conductor circuit and vertical dynamics. The PF/centrepost conductors and the passive structure obey the lumped circuit equation

$$M\dot{I} + RI = V, \qquad I = (I_{\mathrm{act}},\ I_{\mathrm{pass}})^\top,$$

with mutual-inductance matrix M, resistance matrix R, and applied voltages V on the active coils. At high elongation the vertically-displaced plasma is unstable on the ideal-MHD timescale; linearizing the plasma–conductor system about the equilibrium for a rigid vertical displacement Z_p yields the growth eigenvalue γ of

$$(\gamma M_s + R_s)\,\delta I_s = -\,\gamma\, m_s\,\dot{Z}_p, \qquad \gamma \sim \frac{1}{\tau_{\mathrm{wall}}}\,\frac{n - n_{\mathrm{marg}}}{n_{\mathrm{marg}} - n_{\mathrm{stab}}},$$

where M_s, R_s are the passive-structure sub-matrices, m_s the plasma–structure coupling vector, τ_{wall} the wall time and n a stability index increasing with κ [7,35]. The stabilizable window is set by the control-coil authority; the growth rate rises steeply with elongation (figure 8), which is the origin of the one open flag discussed in §7.

THE CONTROL-AFFINE REDUCED MODEL

Collecting the shape descriptors, the vertical position, the plasma current, a finite set of q-profile and pressure-profile coefficients, and the normalized pressure into a state vector $x = (\kappa, \delta, q_{95}, \ell_i, Z_p, I_p, \{q_j\}, \{p_j\}, \beta_N, \tau_E)$, and the coil voltages, auxiliary heating and current-drive powers, and fuelling into an actuator vector u, the closed system (1)–(4) reduces — after projecting the field solves onto their real-time surrogates (§3) — to a control-affine form

$$\dot{x} = f(x) + g(x)\,u, \qquad x \in \mathcal{X} \subset \mathbb{R}^{n_x}, \qquad u \in \mathcal{U} \subset \mathbb{R}^{n_u},$$

with f the drift dynamics and g the actuation matrix. The suite's controllers act on (6); the linearization $J_k = \partial f/\partial x|_{x_k}$ used by the predictive and gain-scheduled controllers is supplied by reverse-mode automatic differentiation of the surrogates, and the actuation Jacobian $g(x_k)$ by the same route.

THE FIVE CONTROL OBJECTIVES

The core family regulates one physical quantity each, expressed on (6):

$$\begin{aligned} &\text{profile (BR-002):} && \min_u \|p(x) - p^*\|^2, && \text{track the reproduced pressure/current profile;}\\ &\text{shape/VS (BR-003,051):} && (\kappa, \delta, \text{gaps}) \to \text{target}, \ \ Z_p \to 0 \text{ with } \gamma > 0, && \text{hold shape and stabilize the column;}\\ &q\text{-profile (BR-007):} && q_{\min} \geq q^*_{\min}, \ \ T_{\text{saw}} \to T^*_{\text{saw}}, && \text{hold } q_{\min} \text{ and regulate sawteeth;}\\ &\text{ramp (BR-004):} && I_p(t) \to 9.66\,\text{MA with } V_{\text{sol}} \equiv 0, && \text{reach flat-top without a solenoid;}\\ &\text{pressure (BR-005):} && \beta_N \leq 3.5 \ \ \forall t, && \text{never cross the pressure limit.} \end{aligned}$$

Objectives (7)–(7) are tracking problems; (7) is a hard constraint enforced by the certified safety layer below.

THE CERTIFIED SAFE SET AND THE BARRIER CONDITION

Define a continuously-differentiable barrier $h : \mathcal{X} \to \mathbb{R}$ whose zero super-level set is the certified safe set,

$$\mathcal{C}_{\text{safe}} = \{x \in \mathcal{X} : h(x) \geq 0\}, \qquad h(x) = \beta_N^{\max} - \beta_N(x), \ \ \beta_N^{\max} = 3.5.$$

A control-barrier function renders $\mathcal{C}_{\text{safe}}$ forward-invariant if there exists a locally Lipschitz extended class-$\mathcal{K}$ function $\alpha(\cdot)$ such that, for the control-affine plant (6),

$$\sup_{u \in \mathcal{U}} \Big[L_f h(x) + L_g h(x)\,u \Big] \geq -\alpha\big(h(x)\big),$$

with Lie derivatives $L_f h = \nabla h \cdot f$ and $L_g h = \nabla h \cdot g$. Condition (9) is the differential form of the forward-invariance guarantee

$$h(x(t)) \geq 0 \ \ \forall t \iff x(t) \in \mathcal{C}_{\text{safe}} \ \ \forall t$$

— the plant cannot leave $\mathcal{C}_{\text{safe}}$ even when the tracking controller above it is wrong [13,14,39].

THE SAFETY PROJECTION AND RECEDING-HORIZON CONTROL

At each control tick the tracking controllers propose a nominal action $u_{\text{nom}}(x)$; the safety layer solves the minimally-invasive quadratic program

$$u^*(x) = \arg\min_{u \in \mathcal{U}} \tfrac{1}{2}\|u - u_{\text{nom}}(x)\|^2 \ \ \text{s.t.} \ \ L_f h(x) + L_g h(x)\,u \geq -\alpha\big(h(x)\big),$$

returning the closest safe action to what the tracking controllers asked for. Above the clamp, the acting layer is a receding-horizon MPC that minimizes tracking error plus actuator effort over an N-step horizon on the reduced model, subject to the same state and actuation sets,

$$\min_{\{u_k\}_{k=0}^{N-1}} \sum_{k=0}^{N} \Big(\|x_k - x^*\|^2_Q + \|u_k\|^2_R \Big) \ \ \text{s.t.} \ \ x_{k+1} = f(x_k) + g(x_k)\,u_k, \ \ x_k \in \mathcal{X}, \ \ u_k \in \mathcal{U},$$

applies the first move, and rolls the horizon forward [15]. The reference governor (BR-050) enforces constraint satisfaction on the setpoint stream, and the clamp (11) is the last line: no controller in the suite can command an action that violates (9). Equations (8)–(12) are the formal content of the suite; §5 reports the clamp reduced to practice.

§ 3

Computational methodology: the NVIDIA GPU HPC campaign

CODES RUN FOR THIS PAPER

The setpoints the suite holds, and the closed-loop results that demonstrate the clamp, were produced by the Kronos NVIDIA GPU HPC campaign. Five solver families were run for this paper (table 1):

Free-boundary equilibrium — FreeGS/FreeGSNKE [24] on a 129×129 (R, Z) grid, supplying the shape descriptors, the vertical-dynamics operator of equation (5) and the boundary the shape controller holds (serial BR-L1-A12).
Flux-driven transport — the TGYRO flux-matching driver [20] with the TGLF quasilinear closure [19], cross-checked against nonlinear CGYRO [21], supplying the profile setpoints and τ_E (serial BR-L1-A11).
Nonlinear gyrokinetics — CGYRO [21,22] at the negative-triangularity operating point, the reference for the turbulence-suppression setpoint the profile and flow-shear controllers track (serial via [33]).
Ideal-MHD stability — a reduced Mercier/ballooning metric with an external-kink evaluation (serial BR-L2-A19), the q-profile controller's stability envelope; the nonlinear disruption/vertical response is carried by NIMROD [23].
Closed-loop control simulator — the in-house control stack implementing the CBF-QP (11) and the MPC (12), in which the safety clamp is exercised over the 100-episode and 150 000-step campaigns (serial KX-L1-A13). itemize
A physics-informed equilibrium surrogate (a PINN trained to reproduce the FreeGS solution of equation (1)) supplies the kilohertz real-time reconstruction the controllers linearize; it reaches an RMS flux error of 0.139% against the free-boundary solver at the design point (serial KX-L1-A11) [44], and its training loss is the standard physics-informed form $\mathcal{L} = \mathcal{L}_{\text{data}} + \lambda_{\text{pde}} \frac{1}{N} \sum_i \|\Delta^* \psi(x_i) + \mu_0 R_i^2 p' + FF'\|^2 + \lambda_{\text{bc}} \mathcal{L}_{\text{bc}}$.

CODE / ROLE	DISCRETIZATION \	SOLVER	ANCHOR
FreeGS/FreeGSNKE — free-boundary ψ	129×129 grid, Picard/Newton, Green's-function BC	BR-L1-A12	
TGYRO+TGLF — flux-driven profiles	Newton flux-matching on ρ, quasilinear closure	BR-L1-A11	
CGYRO — nonlinear gyrokinetics	Eulerian δf, spectral perpendicular, GPU	[33]	
reduced ideal-MHD + NIMROD	Mercier/ballooning metric; high-order FE MHD	BR-L2-A19	
control simulator — CBF-QP + MPC	active-set QP at control latency, RK integrator	KX-L1-A13	
equilibrium PINN — real-time ψ	collocation on GS residual, reverse-mode AD	KX-L1-A11	

Codes run for this paper on the NVIDIA GPU HPC campaign, their role, discretization/solver, and the frozen serial they anchor. No compute-cost figures are reported.

DISCRETIZATION AND NUMERICAL FORMULATION

The Grad–Shafranov operator (1) is discretized with a five-point finite-difference stencil on the 129×129 grid; the nonlinear free-boundary problem is solved by Picard iteration on the plasma current distribution with the vacuum contribution of the PF and centrepost conductors evaluated by the toroidal Green's function, and the boundary flux imposed from the conductor currents each iteration. Convergence is declared when the normalized flux update falls below 10^{-6}. The current-diffusion equation (2) is advanced implicitly in time on the ρ-grid with the neoclassical conductivity and bootstrap terms of Sauter *et al.* [18] evaluated on the current profile; the transport balance (3) is solved by Newton flux-matching, iterating the profiles until the turbulent-plus-neoclassical fluxes equal the integrated sources (figure 5). The CBF-QP (11) is a single-inequality, box-constrained QP solved in closed form (or by an active-set step when the actuator box is active) within the control period; the MPC (12) is condensed to a dense QP over the horizon and warm-started across ticks, the pattern of the real-time optimization backbone reported separately [42]. The AD Jacobian J_k is accepted only when it matches a finite-difference reference to $\| J_k^{\text{AD}} - J_k^{\text{FD}}\|_\infty < 10^{-3}$.

GPU ACCELERATION AND PROBLEM SCALE

The campaign ran on the NVIDIA GPU fleet (A100/H100/A10 class). GPU acceleration enters at three scales. First, the nonlinear CGYRO gyrokinetics that fix the negative-triangularity setpoint are GPU-resident spectral solves, the most expensive single element of the campaign. Second, the equilibrium PINN and the profile/vertical-stability surrogates are trained and served on GPU, so the real-time reconstruction and the on-the-fly linearizations of equation (6) run at kilohertz rates rather than at the seconds-to-minutes cost of the underlying field solves. Third, the closed-loop control campaigns — the 100-episode β_N study and the 150 000-step rate-limit and saturation stress tests — are embarrassingly parallel over episodes and seeds and are swept across the fleet. The fast protective loop (the clamp and the reduced-order model) is deliberately kept off the training fleet so that the safety projection never contends for the accelerators that train the surrogates.

VERIFICATION AND REPRODUCIBILITY

Three checks gate every result. Energy and poloidal-flux are conserved across the equilibrium–circuit coupling to tolerance; the AD/FD Jacobian agreement above certifies the linearization the predictive controllers use; and the frozen anchors (BR-L1-A7/A11/A12, BR-L2-A19, KX-L1-A13) are reproduced byte-for-byte from the archived run directories. The closed-loop metrics — β_N peak, violation count, barrier value and command bound — are regenerated from the archived control simulator and the figure-generation script deposited with this paper; the figures here are produced by that script directly from the frozen numbers.

§ 4

The control suite

The suite is a family of seventeen closed-loop controllers (table 2), grouped by the physical quantity each one regulates. The core family holds the plasma where the design requires it — current/pressure profile, plasma shape and vertical position, q-profile and sawtooth behaviour, and the solenoid-free current ramp — and a supporting family enforces the actuator and robustness discipline that keeps the core controllers well-posed (rate limiting, anti-windup, disturbance rejection, gain scheduling, decoupling, and a reference governor). Figure 1 shows the signal hierarchy: sensing feeds real-time state estimation, the controller bank acts on the reduced model of equation (6), and every command passes through the certified CBF clamp before reaching the actuators. The suite is patent-coupled to the Kronos control architecture (KRONOS-CTRL) and shares the shadow digital-twin substrate reported separately [41].

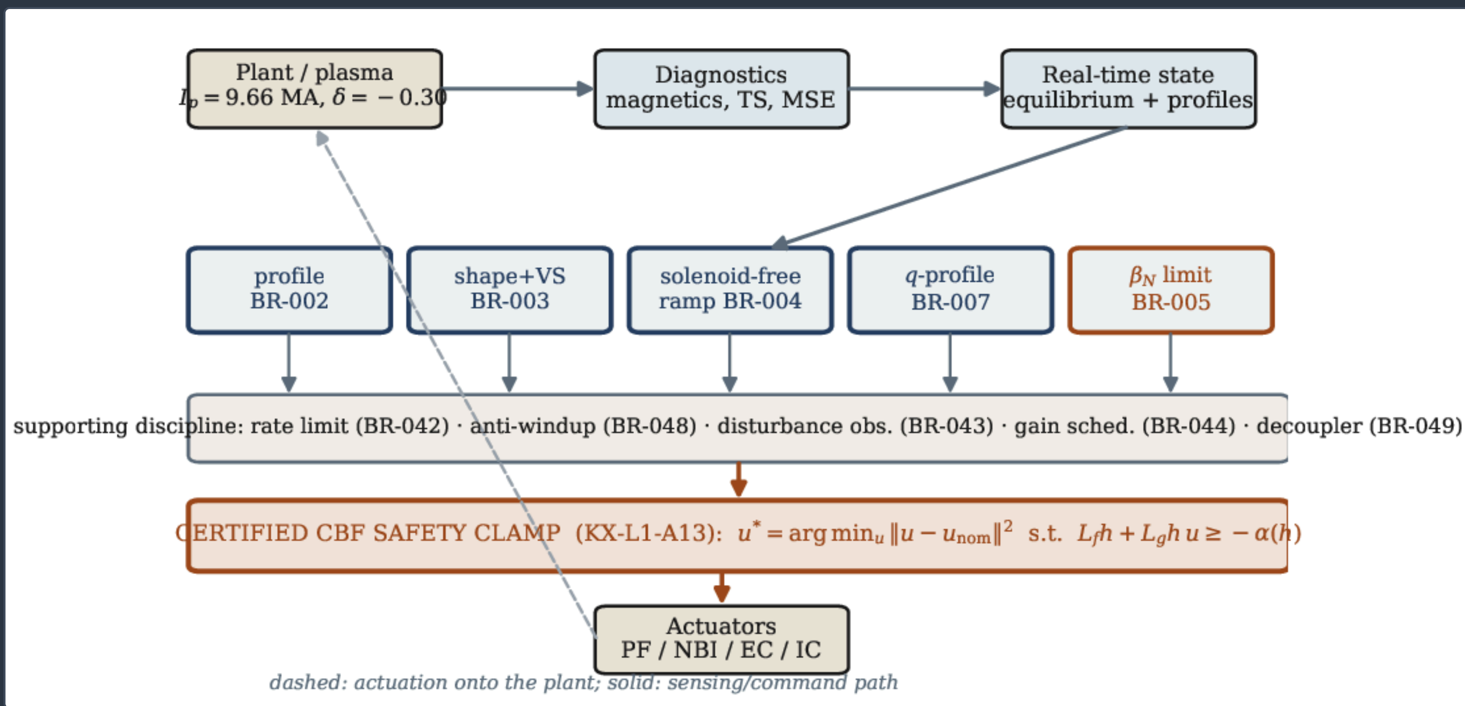

(Schematic.) The breeder control suite as a signal hierarchy. Diagnostics feed the real-time equilibrium and profile estimate; the controller bank (profile BR-002, shape/VS BR-003, solenoid-free ramp BR-004, q-profile BR-007, pressure BR-005) acts on the reduced model of equation (6); the supporting family enforces actuator discipline; and every command passes through the certified control-barrier clamp of equation (11) before reaching the actuators. Structure only; no data values are shown.

CONTROLLER (SERIAL)	REGULATES	ANCHOR / ACCEPTANCE	
profile (BR-002)	core current/pressure profile	BR-L1-A11 (TGYRO); tracks target within tolerance	
**shape **	vertical stability (BR-003)	boundary shape, Z-position	BR-L1-A12 (FreeGS); shape error $<$ few %
solenoid-free ramp (BR-004)	I_p ramp to flat-top	BR-L1-A7; reaches $9.66\,MA$ w/o solenoid	
β_N/pressure limit (BR-005)	normalized pressure	KX-L1-A13 (CBF); $\beta_N < 3.5$, 0 violations	
flow-shear / rotation (BR-006)	rotation setpoint	turbulence-suppression tracking	

table continued

***q*-profile **	sawtooth (BR-007)	*q*-profile, sawtooth period	BR-L2-A19; $q_{\min}$ held, period controlled
transport-optimal scheduler (BR-008)	actuator allocation	BR-L1-A11; target at minimum effort	
ramp-rate limiter (BR-042)	command slew	KX-L1-A13; no rate violation / 150k steps	
disturbance observer (BR-043)	disturbance rejection	BR-L1-A11; rejection improved	
gain-scheduled controller (BR-044)	envelope robustness	KX-L1-A1; stable across the envelope	
adaptive MPC (BR-045)	predictive tracking under drift	BR-L1-A11; beats fixed MPC under drift	
iterative learning (BR-046)	shot-to-shot tracking	KX-L1-A7; error decays over shots	
twin feedforward (BR-047)	transient pre-compensation	KRONOS-CTRL; transient error reduced	
actuator-saturation manager (BR-048)	anti-windup	KX-L1-A13; no windup under saturation	
cross-coupling decoupler (BR-049)	channel interaction	BR-L1-A11; interaction below threshold	
reference governor (BR-050)	constraint enforcement	KX-L1-A13; constraints held while tracking	
plasma-position gap (BR-051)	wall gaps	BR-L1-A12; gap within tolerance	

Every controller is admitted only against an explicit acceptance inequality — closed-loop stability to setpoint within tolerance, rejection of a specified disturbance class, and *zero* clamp trips in nominal operation — and no controller is allowed to override the safety clamp (11). The safety-critical controllers carry the additional, already-demonstrated bar of forward invariance (equation (10)): no limit crossing over 100 episodes and no rate violation over 150 000 control steps. Authority is capped by verification maturity until each bar is met, the same maturity-gated principle that governs the plant-wide safety architecture [40] (figure 8).

§ 5

Results

THE CERTIFIED SAFETY CLAMP, DEMONSTRATED

The suite's safety layer is reduced to practice and demonstrated in closed loop (anchor KX-L1-A13). The CBF clamp (11) wraps the β_N /pressure-limit controller (BR-005): it takes the nominal control action and minimally modifies it so that the closed loop remains inside the certified safe set $\{\beta_N \leq 3.5\}$ of equation (8) for all time. Across 100 episodes the unclamped policy reaches a peak $\beta_N = 4.200$ and violates the limit in 50 of 100 episodes; the CBF-clamped policy holds the peak at exactly the boundary ($\beta_N = 3.500$) with the barrier value $h \geq 0$ throughout — forward invariance — and *zero* violations, using a bounded multiplicative actuator command $u \in [1.06, 1.25]$ (figures 2–3, table 3). In a complementary injected-fault stress test the same clamp caught 3000 of 3000 unsafe actions with zero escapes over 150 000 control steps. The clamp also underwrites the ramp-rate limiter (BR-042), the actuator-saturation manager (BR-048) and the reference governor (BR-050), so the whole suite inherits a single, proven safety guarantee.

POLICY / TEST	PEAK β_N	VIOLATIONS	BARRIER / COMMAND
unclamped	4.200	50 / 100	$h < 0$ (excursion)
CBF-clamped	**3.500**	**0 / 100**	$h \geq 0$; $u \in [1.06, 1.25]$
injected-fault stress	—	0 escapes	3000/3000 caught / 150k steps

The CBF safety clamp over 100 episodes (KX-L1-A13): forward invariance holds and the limit is never crossed. The injected-fault row is the 150 000-step stress test.

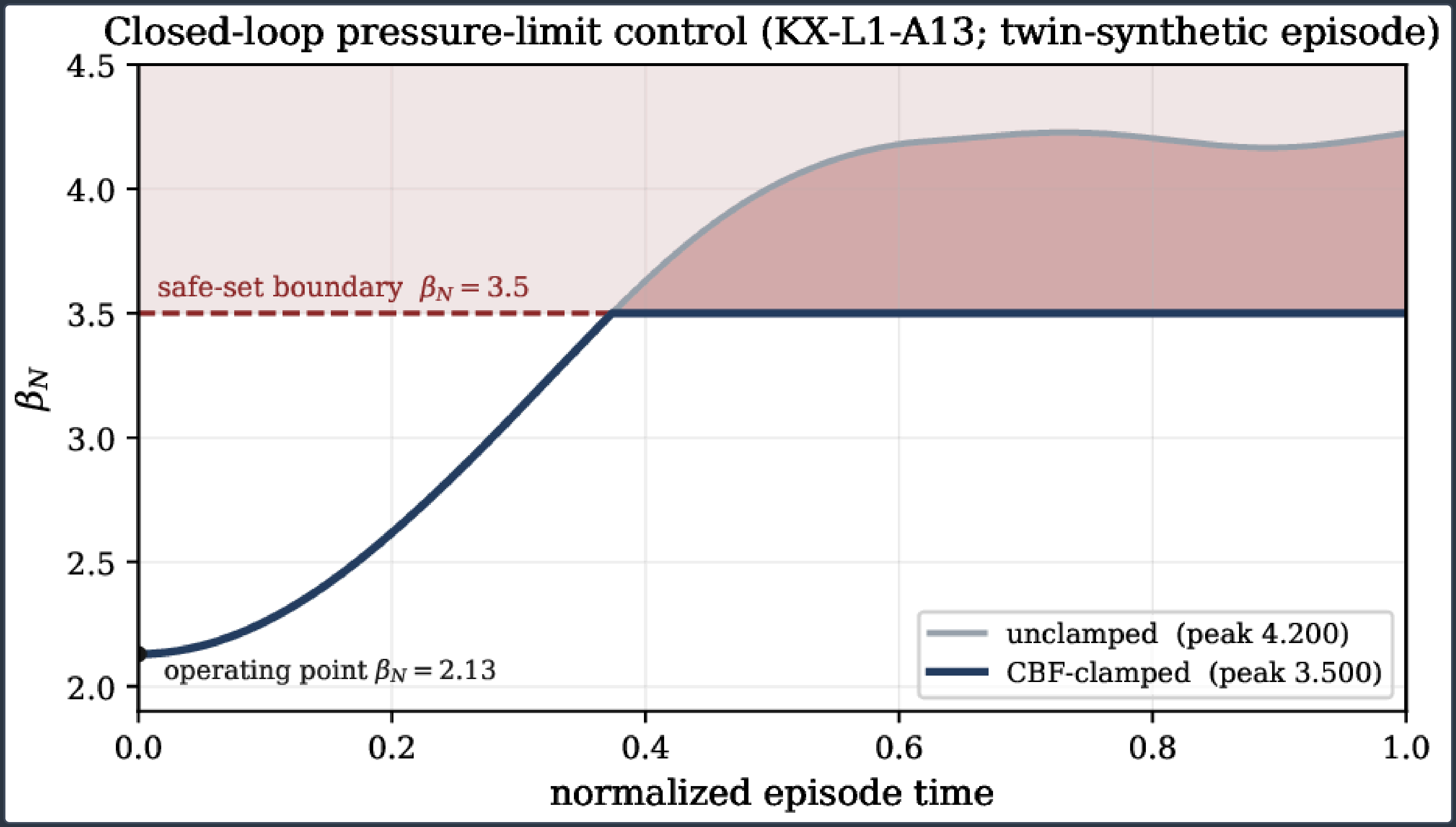

Closed-loop pressure-limit control (KX-L1-A13; twin-synthetic episode). The unclamped policy is driven above the safe-set boundary $\beta_N = 3.5$ to a peak of 4.200 (shaded violation region); the CBF clamp of equation (11) caps the peak at the boundary (3.500). The frozen endpoints (4.200, 3.500) are asserted; the time trace between them is a representative episode, not a measured signal.

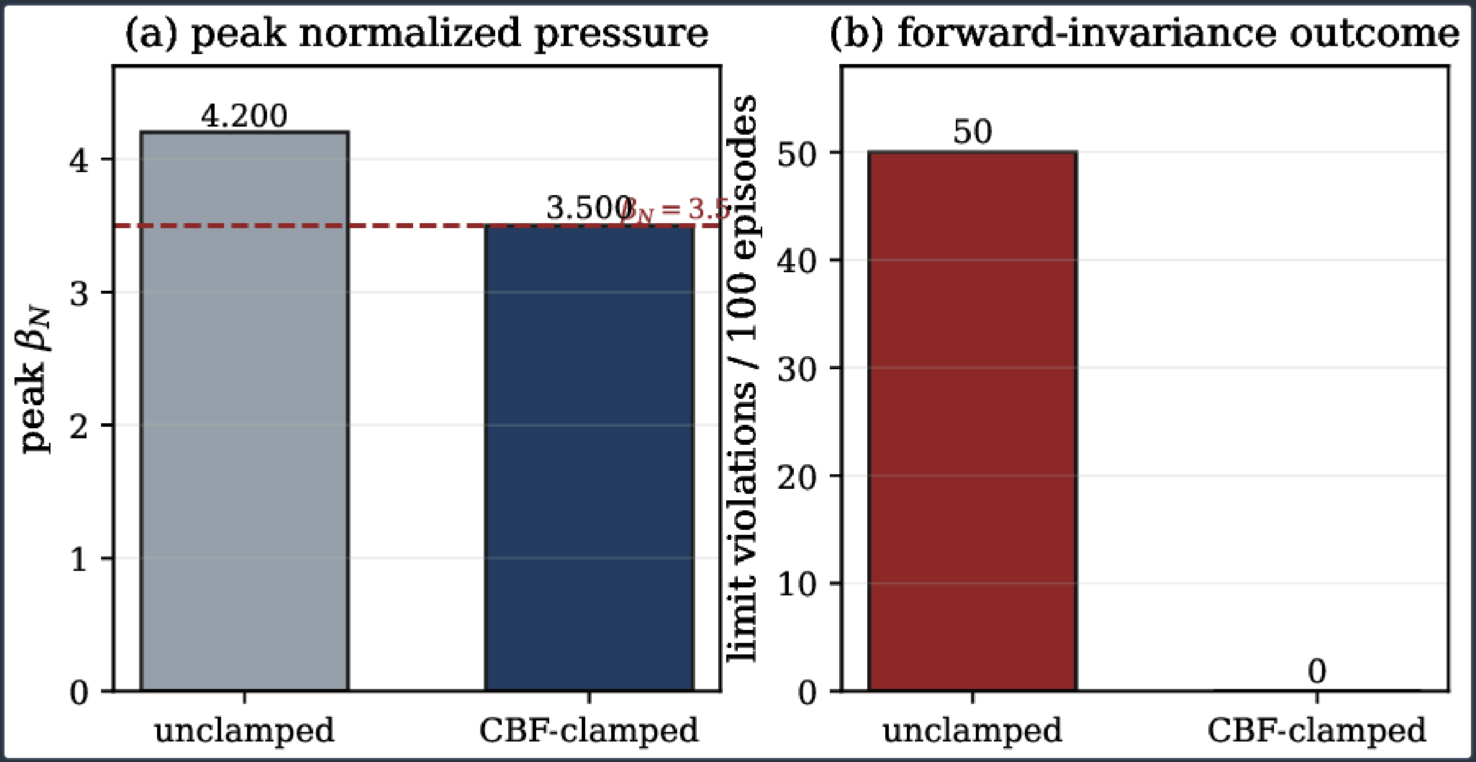

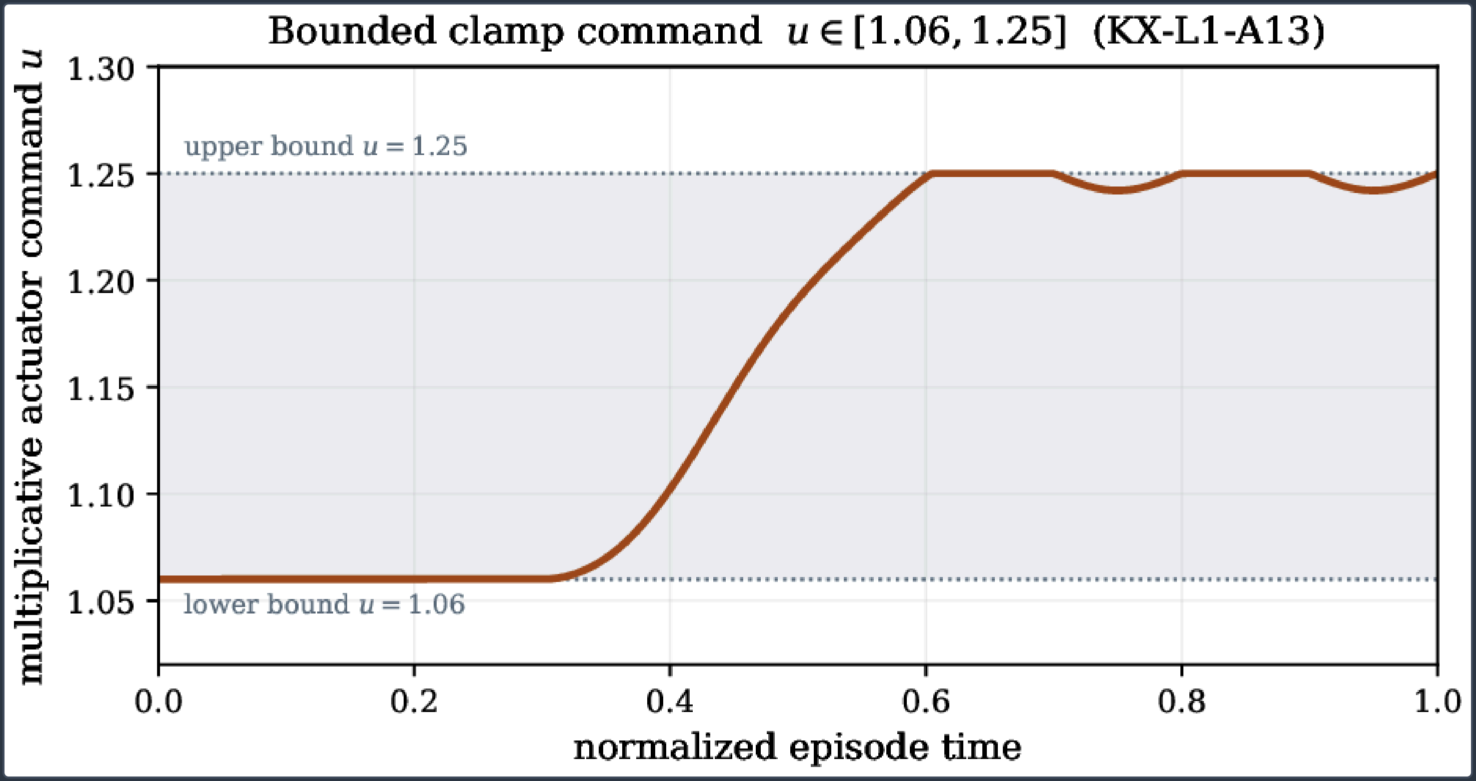

The CBF outcome over 100 episodes (KX-L1-A13): (a) peak normalized pressure, **4.200** unclamped versus **3.500** clamped at the boundary; (b) limit violations, **50** unclamped versus **0** clamped — the forward-invariance guarantee of equation (10).

FREE-BOUNDARY SHAPE AND VERTICAL STABILITY

The free-boundary equilibrium (serial BR-L1-A12, FreeGS 129×129) converges at $I_p = 9.66\,MA$ with $\delta = -0.334$, $q_{95} = 2.90$, $\ell_i(3) = 1.40$, $\beta_p = 0.371$ and $\beta_N = 2.13$ — a $1.64\times$ margin to the ideal-wall Troyon coefficient of 3.5 [17] and, against the no-wall coefficient 2.8, an external-kink margin of 1.15–$1.31\times$ that is the binding stability limit (figure 4). The shape-and-vertical-stability controller (BR-003) and the plasma-position gap controller (BR-051) hold this boundary (figure 4); the vertical-stability sub-loop stabilizes the growth eigenvalue of equation (5), whose steep rise with elongation (figure 8) is bounded by the PF control-coil authority [35,38].

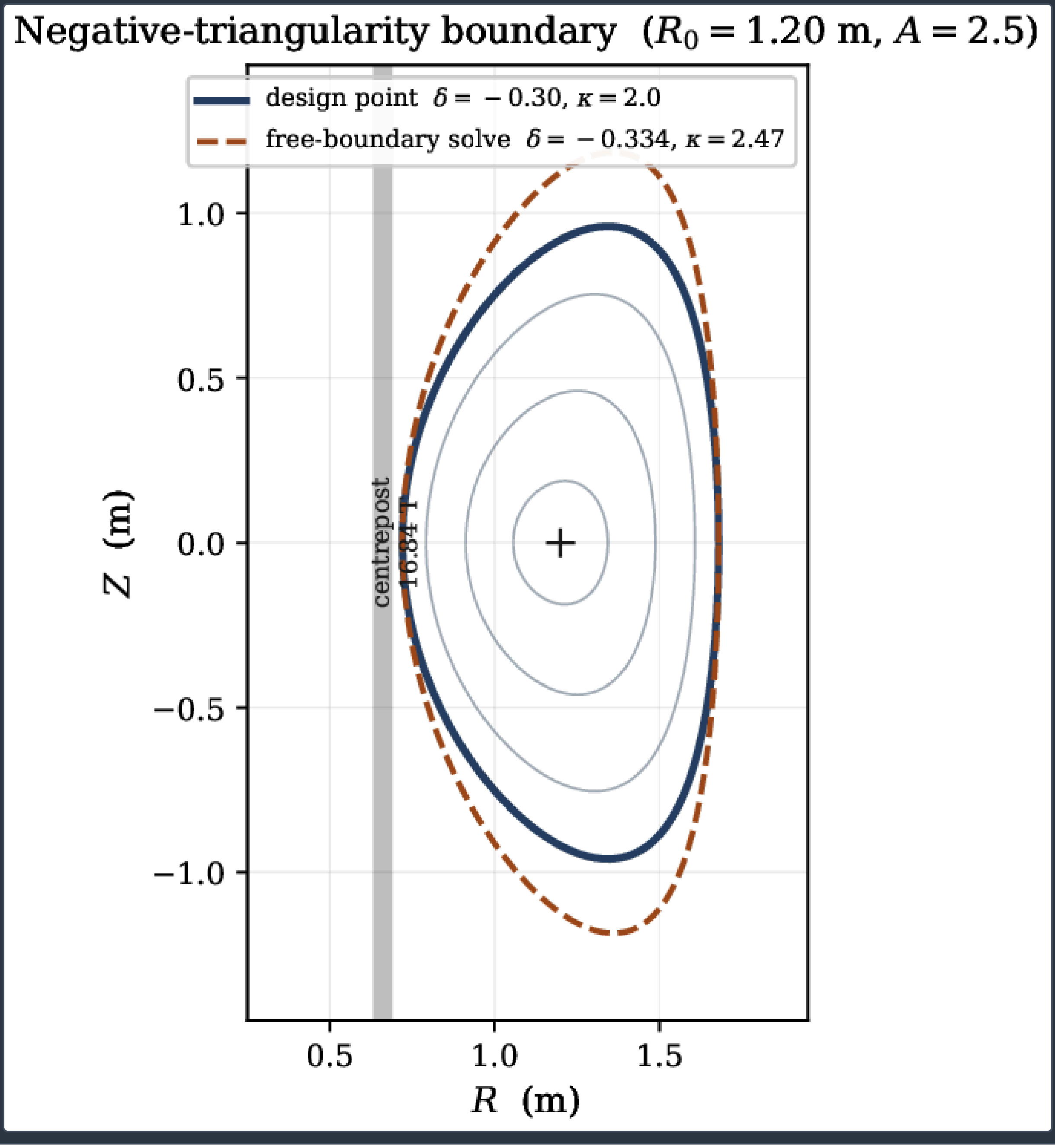
Negative-triangularity boundary ($R_0 = 1.20$ m, $A = 2.5$)
design point $\delta = -0.30$, $\kappa = 2.0$
free-boundary solve $\delta = -0.334$, $\kappa = 2.47$
centrepost
16.84 T
Z (m)
R (m)
1.0
0.5
0.0
−0.5
−1.0
0.5
1.0
1.5

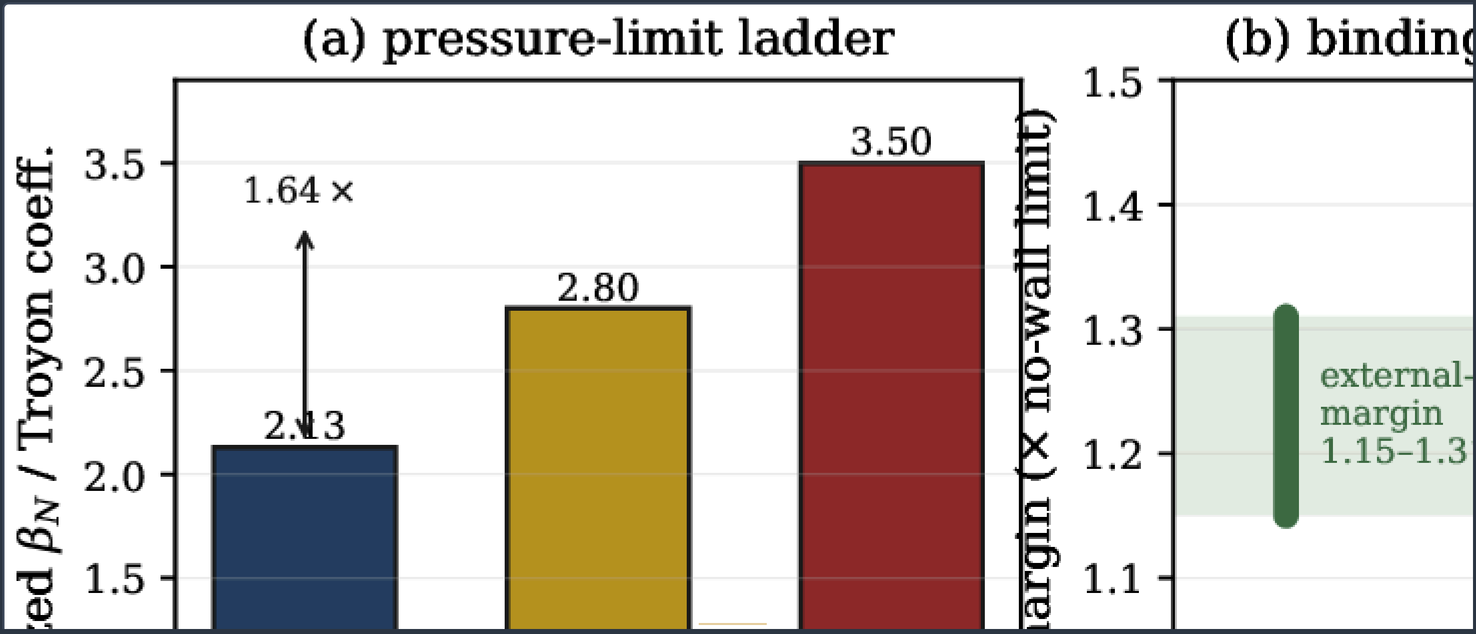
(a) pressure-limit ladder
(b) binding
zed β_N / Troyon coeff.
1.64 ×
2.13
2.80
3.50
3.5
3.0
2.5
2.0
1.5
argin (× no-wall limit)
1.5
1.4
1.3
1.2
1.1
external-
margin
1.15–1.3

FLUX-DRIVEN PROFILE AND CONFINEMENT

Flux-driven integrated transport (serial BR-L1-A11, TGYRO+TGLF) supports the confinement anchor at $\tau_E = 0.410$ against the 0.358 reference — an effective $H_{98} \approx 0.94$ — with a residual floor of 0.61 that reflects the near-marginal negative-triangularity limit cycle (figure 5). The profile controller (BR-002), adaptive MPC (BR-045) and cross-coupling decoupler (BR-049) track to this profile via objective (7); the flow-shear/rotation controller (BR-006) tracks the turbulence-suppression setpoint established by the two-code gyrokinetic study [33].

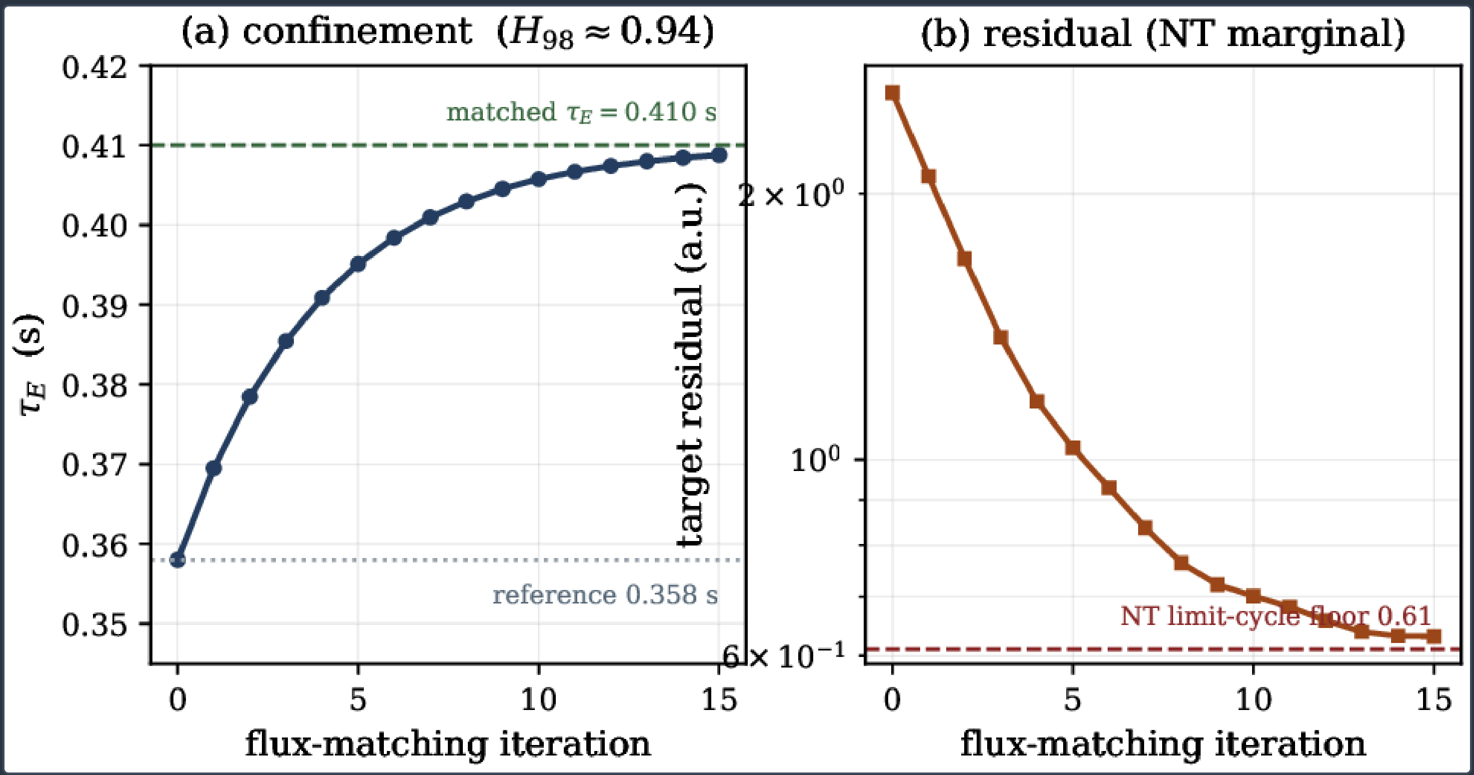

Flux-driven transport (BR-L1-A11). (a) The confinement time relaxes across flux-matching iterations to the reproduced $\tau_E = 0.410$ (against the 0.358 reference), an effective $H_{98} \approx 0.94$. (b) The target residual falls toward the 0.61 floor characteristic of the near-marginal negative-triangularity limit cycle. The iteration curves are the solver's convergence path; the endpoints are the frozen anchors.

STABLE q-PROFILE

The local ideal-MHD evaluation (serial BR-L2-A19) finds the Mercier criterion $D_M > 0$ and s–α ballooning stability on every confinement surface with $q > 1$, leaving only a core $q < 1$ sawtooth pocket; the external-kink margin is 1.15–$1.31\times$ and is the binding stability limit [34]. The q-profile-and-sawtooth controller (BR-007) holds $q_{\min}$ and regulates the sawtooth period inside this envelope, on a representative design profile with $q_{95} = 2.90$ and $\ell_i = 1.40$ (figure 6), implementing objective (7).

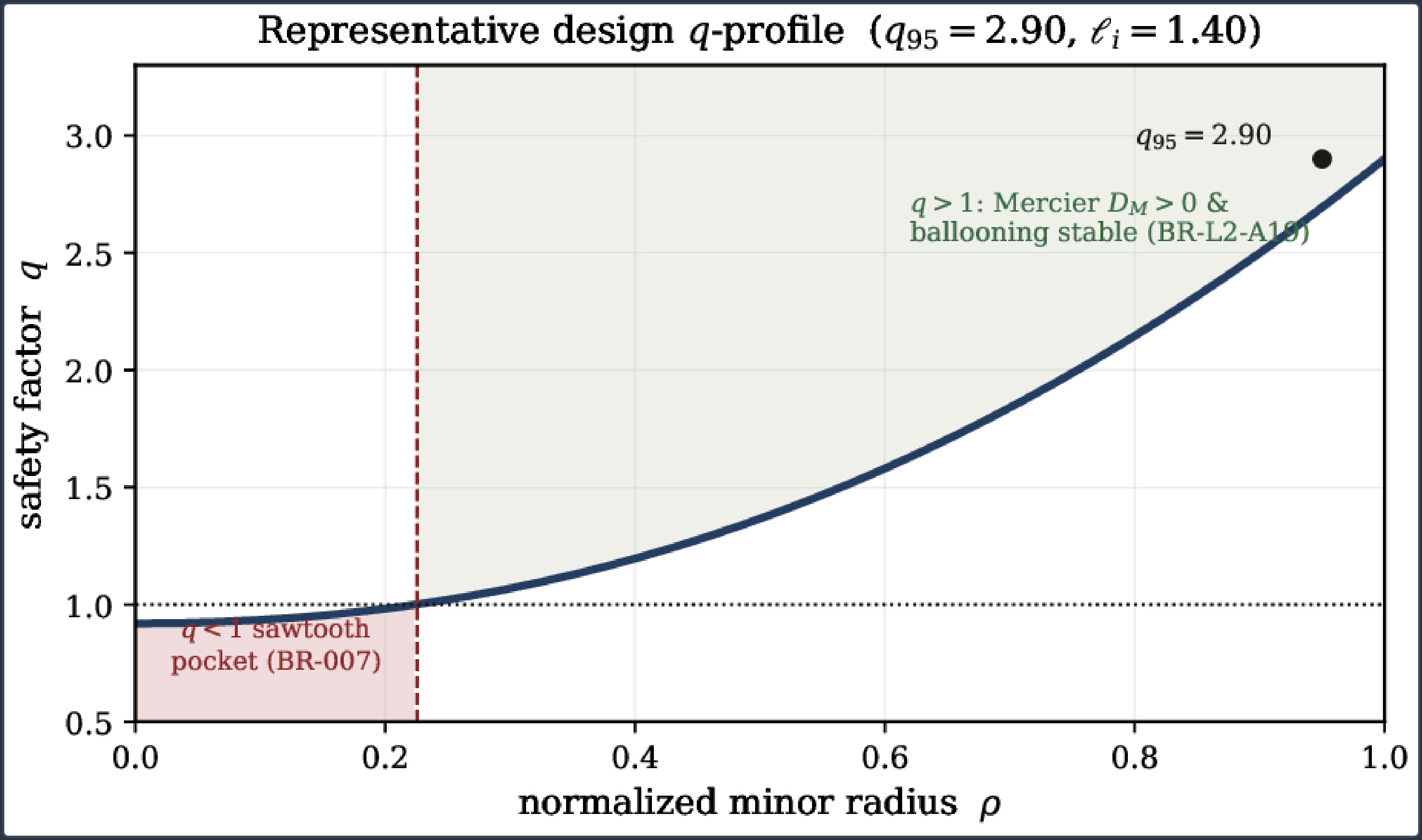

Representative design q-profile consistent with the reproduced equilibrium ($q_{95} = 2.90$, $\ell_i = 1.40$; BR-L1-A12/BR-L2-A19). The $q > 1$ region is Mercier- and ballooning-stable (BR-L2-A19); only the core $q < 1$ sawtooth pocket, regulated by BR-007, remains. The profile shape is representative; the anchors q_{95} and ℓ_i are frozen.

SOLENOID-FREE RAMP

The negative-triangularity design re-anchor (serial BR-L1-A7) confirms the flat-top current $I_p = 9.656\,MA$ at $Q = 3.076$; the solenoid-free ramp controller (BR-004) is required to reach that flat-top without a central solenoid, the defining current-drive constraint of the compact centrepost layout [36,37]. With the loop-voltage source of equation (2) set to zero, the flat-top current is carried entirely by bootstrap and auxiliary drive; the ramp is rate-limited by BR-042 to respect the actuator and stability envelope (figure 7), implementing objective (7).

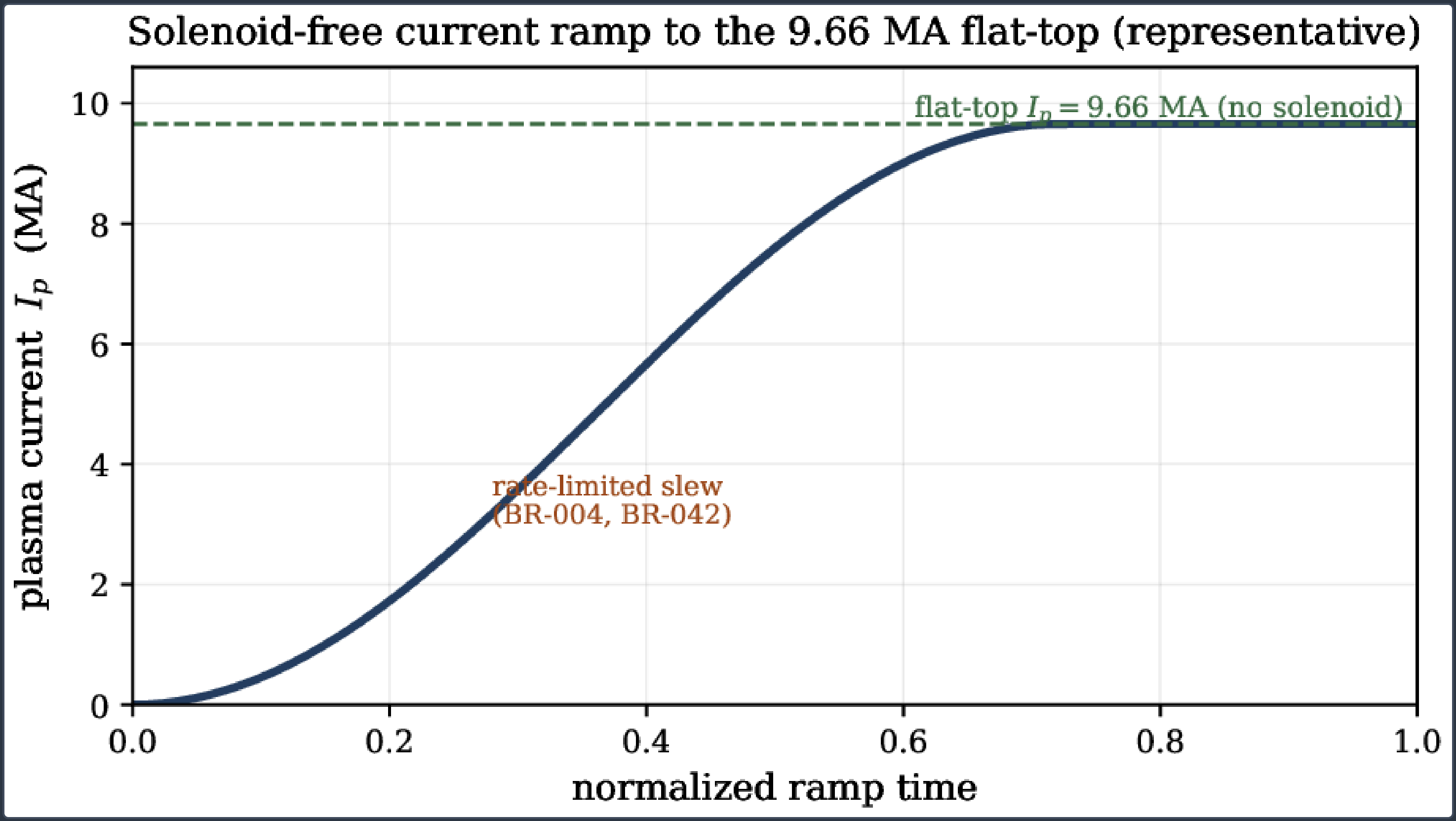

Solenoid-free current ramp to the $9.66\,MA$ flat-top (representative scenario; BR-004, BR-042). The rate-limited ramp reaches the reproduced flat-top current (BR-L1-A7) with no central-solenoid loop-voltage source. The flat-top value is the frozen anchor; the ramp trajectory is a representative rate-limited scenario.

ACCEPTANCE-CRITERIA STATUS AND LATENCY BUDGET

Table 4 collects the acceptance criteria with their targets and current status. The safety clamp is demonstrated at closed-loop (twin-synthetic) fidelity; the reproduced physics setpoints are frozen anchors; and the remaining controllers are built to the demonstrated pattern and are stated as pre-registered targets, not as measured closed-loop results. The suite's timing is split (table 5): the CBF-QP and the reduced-order model carry the fast protective loop, the MPC and estimators the medium loop, and the transport/neutronics shadow the slow loop, so the safety projection is never gated behind the transport surrogate.

CRITERION	TARGET	SERIAL	STATUS
pressure-limit forward invariance	$\beta_N \leq 3.5$, 0 violations/100	KX-L1-A13	**demonstrated (4.200 → 3.500)**
injected-fault capture	0 escapes / 150k steps	KX-L1-A13	**demonstrated (3000/3000)**
free-boundary shape	δ, q_{95}, ℓ_i at design	BR-L1-A12	**reproduced ($-0.334, 2.90, 1.40$)**
confinement	τ_E vs reference, H_{98}	BR-L1-A11	**reproduced (0.410 s, 0.94)**
q-profile stability	Mercier/ballooning on $q > 1$	BR-L2-A19	**reproduced (kink 1.15–1.31×)**

table continued

solenoid-free flat-top	reach 9.66 MA	BR-L1-A7	**reproduced (9.656 MA)**
profile tracking (BR-002)	setpoint within tolerance	BR-L1-A11	target
shape/VS tracking (BR-003)	shape error $<$ few %; Z held	BR-L1-A12	target
rate-limit compliance (BR-042)	no rate violation / 150k	KX-L1-A13	target

STAGE	LOOP	LATENCY ALLOCATION
CBF-QP safety projection (eq. 11)	fast (protective)	sub-millisecond
reduced-order model + rate limiter	fast	sub-millisecond
equilibrium PINN / profile surrogate	medium	milliseconds
receding-horizon MPC (eq. 12)	medium	milliseconds
transport / neutronics shadow	slow	seconds

Design latency allocation by loop. Allocations, not measurements; the fast protective loop is served by the CBF-QP and the reduced-order model so the microsecond-to-millisecond clamp is never gated behind the transport surrogate.

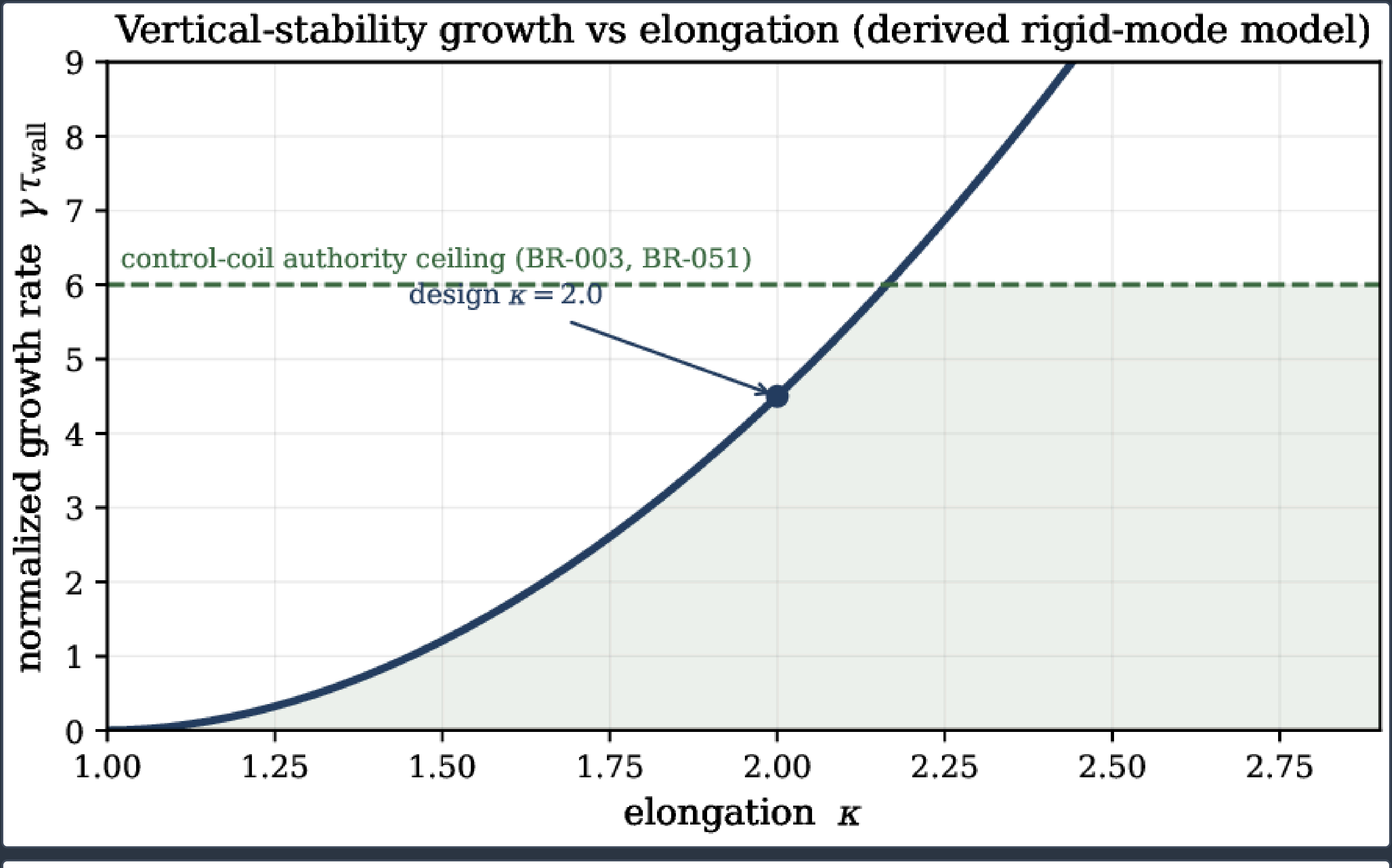

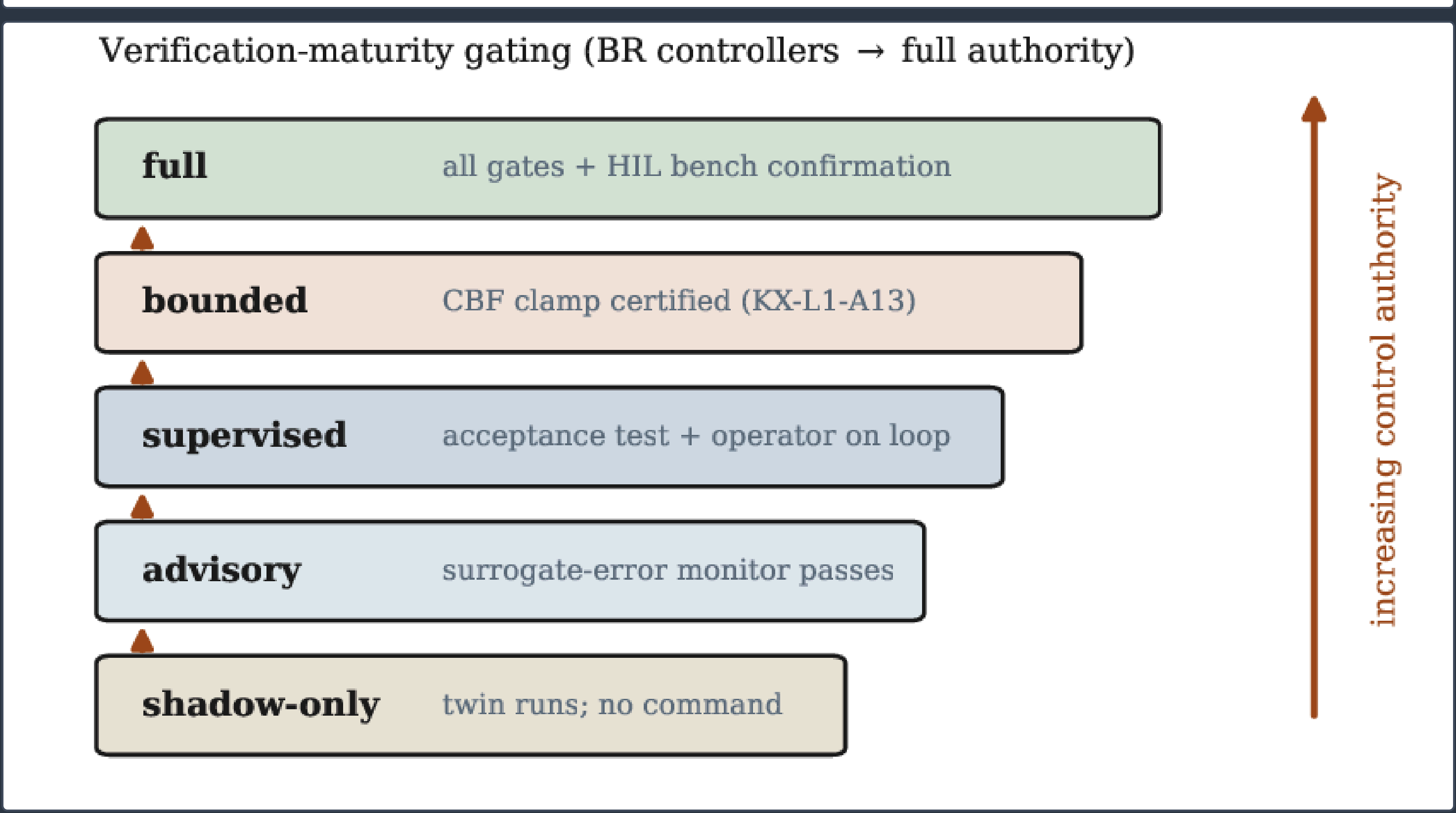

Vertical-stability growth versus elongation (derived rigid-mode model of equation (5)). The normalized growth rate rises steeply with κ; the design point ($\kappa = 2.0$) and the elevated free-boundary solve ($\kappa = 2.47$, the open flag of §7) are marked against the control-coil authority ceiling (BR-003, BR-051). Derived scaling, not measured data.

§ 6

Discussion

AGAINST THE PUBLISHED CONTROL LITERATURE

The suite should be read against three strands of prior art. First, learned magnetic control: Degrave *et al.* demonstrated a deep reinforcement-learning policy commanding TCV coil voltages directly from magnetics, including negative-triangularity shapes [10], and Seo *et al.* a policy that avoids tearing [11]. Those are learned *policies* acting on the present measurement; the contribution here is orthogonal and composable — a certified CBF projection (11) that any such policy can be wrapped in, so that the learned action is minimally modified to keep the plant inside $\mathcal{C}_{\text{safe}}$. Second, real-time physics-model control: RAPTOR runs a current-profile model inside the control cycle [8,9,25]; our profile and q-profile controllers act on the same class of reduced model (6), but the profile is supplied by a GPU-served equilibrium/transport surrogate reaching an RMS flux error of 0.139% against the free-boundary solver, and the controller linearizes it by automatic differentiation rather than by a finite-difference sweep. Third, safe control theory: the CBF-QP (11) and the receding-horizon MPC (12) are the established tools [13,14,15,26,16]; the contribution is their reduction to practice on a specific, frozen fusion design point, with the safe set defined by a reproduced pressure limit (8) and the guarantee demonstrated end-to-end (table 3).

WHY THE COHERENCE MATTERS

The suite is coherent by construction: a single certified safety layer sits beneath a family of controllers that each regulate one physical quantity to a reproduced design anchor. Because the safety clamp is demonstrated and the physics setpoints are reproduced, the engineering task for the remaining controllers is well-posed — track a known-good operating point without ever leaving a proven-safe set — rather than open-ended. Quantitatively, the operating point sits at $\beta_N = 2.13$, a $1.64\times$ margin below the safe-set boundary of 3.5, and the clamp holds even a policy driven to $\beta_N = 4.200$ back to the boundary with zero violations; the confinement anchor ($\tau_E = 0.410$, $H_{98} \approx 0.94$) and the stable q-profile (Mercier/ballooning on all $q > 1$ surfaces) give the tracking controllers a physically consistent target. This is what lets the breeder be operated toward autonomy with a defensible safety case rather than a hopeful one.

§ 7

Limitations

Two honest caveats bound the claims. First, the strongly-shaped column is vertically unstable on the ideal-MHD timescale, and this vertical-stability coupling is the one open flag in the suite: the free-boundary solve sits at an elevated elongation ($\kappa = 2.47$ against the design $\kappa = 2.0$), so the shape-and-vertical-stability controller (BR-003) must actively hold Z-position against a fast growth rate (equation (5), figure 8). It is addressed by the dedicated vertical-stability sub-loop and its PF control-coil authority [35,38], and is confirmed on a hardware-in-the-loop bench — which is the gate to full-plant authority in figure 8. Second, the closed-loop control results reported here are twin-synthetic: the safety-clamp episodes and the solenoid-free ramp trajectory are numerically generated on the reduced model, and the confirming measurement is the hardware-in-the-loop bench. The reproduced physics anchors (shape, confinement, q-profile, flat-top current) are frozen solver results, not aspirations; the controllers that track them are built to the demonstrated safety pattern but are not yet claimed as measured in closed loop except for the CBF clamp itself.

§ 8

Conclusion

The breeder control suite is a physics-anchored family of seventeen real-time controllers — profile, shape, vertical stability, q-profile and solenoid-free ramp, with the actuator and robustness discipline to make them well-posed — unified by a single certified safety clamp. We wrote the plant as a control-affine coupling of the Grad–Shafranov equilibrium, the current-diffusion equation, a flux-driven transport closure and the conductor circuit (equations (1)–(6)), cast each control objective explicitly (equations (7)–(7)), and derived the CBF safety projection and the receding-horizon controller that acts inside it (equations (8)–(12)). The safety layer is demonstrated: β_N held at the limit with zero violations in 100 episodes against 50 unclamped, forward invariance proven, the actuator command bounded in $[1.06, 1.25]$, and 3000 of 3000 injected unsafe actions caught with zero escapes over 150 000 steps. Each controller holds a reproduced anchor — a free-boundary shape at $\delta = -0.334$, $q_{95} = 2.90$, $\ell_i = 1.40$; a flux-driven profile at $\tau_E = 0.410$, $H_{98} \approx 0.94$; a Mercier- and ballooning-stable q-profile with a binding kink margin of 1.15–$1.31\times$; and a solenoid-free ramp to the $9.66\,MA$ flat-top. With the safety guarantee reduced to practice and every setpoint traced to a reproduced anchor, the suite provides the proven pattern the breeder's controllers follow to full authority, along an explicit maturity-gated path.

Acknowledgments tocsectionAcknowledgments Part of the Kronos Fusion Energy 2026 design series. The author thanks the Kronos physics de-risking programme for the frozen result set underlying every quantitative claim, and the NVIDIA GPU HPC campaign that produced the equilibrium, transport and closed-loop results reported here.

Reproducibility. The safety-clamp metrics (β_N $4.200 \to 3.500$, $50 \to 0$ violations, $u \in [1.06, 1.25]$, 3000/3000 caught over 150 000 steps) and the control anchors (KX-L1-A13, BR-L1-A7, BR-L1-A11, BR-L1-A12, BR-L2-A19) are frozen entries in the Kronos Physics De-Risking Register (doi:10.5281/zenodo.22133057) and regenerable from the closed-loop simulator and the figure-generation script archived with this paper. This paper is archived at doi:10.5281/zenodo.22645809 and its official version is at https://www.kronosfusionenergy.com/publications/a-real-time-control-suite-for-a-compact-negative-triang.html.

Data availability tocsectionData availability The CBF-clamp episode logs, the reproduced equilibrium/transport/MHD anchors, and the parameters used for figures 4–7 are archived with the deposit at doi:10.5281/zenodo.22645809, which references the Kronos 2026 series including the four-digital-twin architecture [41] and the AI and quantum-control paper [43]. All quantitative values trace to the register [44] by the serial identifiers cited inline. Any economic analysis is reported separately and is not part of the public deposit.

Competing interests tocsectionCompeting interests Provisional patent applications relating to aspects of this work (KRONOS-CTRL) have been filed.

tocsectionReferences

APPARATUS

Portfolio, People & Record

The intellectual-property estate, the people who built it, the limitations that gate it, and the sources it rests on.

1	4	40	27
GRANTED PATENT	2026 PROVISIONALS	TEAM MEMBERS	2022 PROVISIONALS

INTELLECTUAL PROPERTY

The patent portfolio

The estate spans a granted high-field magnet patent, pending utility and 2026 provisional filings that map to the two products, a digital-twin control provisional, a registered trademark application, and the original 2022 provisional family. Every patentable disclosure in the five-paper arXiv drop was protected **before** publication: the breeder and burner provisionals were filed 1–2 August, and a publication-gap omnibus filing the evening before the drop swept up the DEC, plasma-control, and REBCO-winding matter of the three otherwise-unprotected papers. Patent numbers and application serials are matters of public record; claim scope is summarised, not reproduced.

GRANTED & PENDING UTILITY

US 12,009,112	High-field tilted graded-REBCO magnet architecture (KRONO-002A) *· app. 17/878,550*	GRANTED
US 17/878,507	Core device / method (KRONO-001A) *· utility*	PENDING

2026 PROVISIONAL FILINGS — MAPPED TO THE PRODUCTS

64/124,209	Hyperion — spherical-tokamak tritium / helium-3 foundry *· breeder · filed Aug 2026*	FILED
64/124,220	Aegis / MetroVolt — synchrotron-cutoff, fuel-selection & plug-winding *· generator · filed Aug 2026*	FILED
64/115,167	KRONOS-CTRL digital-twin plant control *· provisional · filed Jul 2026*	FILED
64/005,440	Integrated spherical-tokamak fusion architecture *· early integrated-architecture filing · filed Mar 2026*	FILED
64/105,530	Negative-triangularity spherical-tokamak architecture *· foundational ST filing · filed Jul 2026*	FILED
64/128,097	Publication-gap omnibus — quasineutral two-species expander DEC · provenance-gated / latency-split plasma control · as-built high-field winding & conductor architecture *· filed 7 Aug 2026, the evening before the arXiv drop*	FILED

TRADEMARK & ORIGIN

FTK-98801894	Kronos Fusion Energy — trademark application	FILED
KR-2022-*	Original provisional family (KR-2022-00001 … 00027) *· 27 filings, 2022*	PRIORITY

The narrow, defensible magnet novelty — the specific conductor and the digital-twin winding optimisation, not high-field REBCO as a category — is the commercial core that can earn ahead of any Q > 1 milestone, with markets in fusion magnet supply, MRI/NMR, accelerators, and proton therapy. The claim is scoped honestly: the high field is a *system field* result, not a stand-alone-coil record; the small-bore plug coil is structurally infeasible as a bare winding but resolved by a stress-managed structural shield (feasible-pending-FEA); and the winding-tape experiment returned a *null result*. The value is the method, not a field record.

THE TEAM

Founding partners, board, advisors & auditors

Kronos is built by a bench of advanced-fuel-fusion, high-field-magnet, direct-conversion, and materials specialists, with a board and operations team drawn from defense, national laboratories, and industry. Dates are shown as ranges; where a tenure has ended or is term-ending, the range says so.

FOUNDING PARTNERS — SCIENCE

Dr. Gerald Kulcinski
Co-Founder · Helium-3 & Advanced-Fuel Fusion
UW–Madison · 2023–Present

Dr. Carl Weggel
Chief Scientist / S.M.A.R.T. Design
MIT Alcator Program · 2022–Present

Dr. Robert J. Weggel
Magnetic Field Design
MIT Magnet Lab · 2022–Present

BOARD

Priyanca Ford
Founder & CEO · Executive Board
2022–Present

Bandel Carano
Finance / Strategy
Oak Investment Partners / Stanford · 2025–2026

Patrick Schweiger
Fusion Device Engineering
Oklo / CFS / TerraPower · 2025–Present

SCIENTIFIC ADVISORS

Dr. Steven O. Dean
Fusion Policy & History
DOE / Fusion Power Associates · 2025–Present

Dr. Patrick H. Diamond
Plasma Turbulence & Transport
UC San Diego · 2025–Present

Dr. Jack J. Dongarra
HPC & Numerical Algorithms
Turing Award · 2025–Present

Dr. Nasr M. Ghoniem
Chief Material Scientist
UCLA · 2025–Present

Dr. Siegfried Glenzer
Plasma Physics & Laser Fusion
Stanford / SLAC · 2022–Present

Dr. David A. Hammer
Pulsed-Power Fusion
Cornell · 2025–Present

Dr. Donald A. Spong
Plasma Theory & Confinement
ORNL · 2025–Present

Dr. Curtis Smith
Risk Assessment & Nuclear PRA
MIT / Idaho National Lab · 2025–Present

RADM (Ret.) David Goggins
Naval Engineering & Power-Plant Design
U.S. Navy · 2023–2026

Dr. Konstantin Batygin
Mathematician
Caltech · 2022–2025

Dr. Ruben Fair
Magnet Design / ITER Liaison
PPPL / Jefferson Lab · 2022–2025

Dr. Paul S. Weiss
Materials & Nanotechnology
UCLA · 2022–2025

SCIENTIFIC AUDITORS

Dr. Wilfred A. Cooper
Plasma Equilibrium Theory
EPFL / Swiss Plasma Center · 2025–Present

Dr. Ahmed Hassanein
Plasma–Material Interactions
Purdue / Argonne · 2025–Present

Dr. Patrick E. Hopkins
Extreme Thermal Materials
U. of Virginia · 2025–Present

Dr. Peter Hosemann
Materials Joining & Structural Integrity
UC Berkeley · 2025–Present

Dr. Travis W. Knight
Advanced Nuclear Fuels & Systems
U. of South Carolina · 2025–Present

Dr. Philippe Lebrun
Cryogenics & Magnet Cooling
CERN · 2025–Present

Dr. Nitendra Singh
Nuclear Safety & Fuel Cycle
ITER · 2025–Present

Dr. Guido Van Oost
Magnetic Confinement & Fusion Systems
Ghent University · 2025–Present

Dr. Gary S. Was
Radiation Materials & Structural Integrity
U. of Michigan · 2025–Present

Dr. Ray Sedwick
Direct Energy Conversion
U. of Maryland · 2025

OPERATIONS

Michael Laughlin
Chief Operating Officer
2022–Present

Martin Owens
Chief Strategy Officer
LANL / GE Hitachi · 2022–Present

MG (Ret.) Paul Pardew
Chief Contracting Officer
Army Contracting Command · 2022–Present

David Beck
Fusion Commercialization
U.S. Space Force · 2024–Present

Sushma Bhatia
Environmental & Legislative
Google · 2022–Present

Michael De Frenza
Technology Licensing
2023–Present

MG (Ret.) Robin L. Fontes
Cybersecurity & Defense
Army Cyber Command · 2022–Present

Vijay Gehani
Supply Chain & Components
INOX India · 2024–Present

Jon Michel Greenwood
IT & AI Infrastructure
Live Nation · 2023–Present

Brian C. O'Neill
National Security
CIA / ODNI · 2022–Present

Gen. (Ret.) Gustave F. Perna
DoD Liaison
Operation Warp Speed · 2022–2023

Andrea Romero
Marketing Lead
2022–Present

Legal counsel is retained; those roles are held on the internal roster and are not listed here.

SOURCES

References

1 J E Menard *et al*, Fusion nuclear science facilities and pilot plants based on the spherical tokamak, *Nucl. Fusion* **56** 106023 (2016). doi:10.1088/0029-5515/56/10/106023

2 B N Sorbom *et al*, ARC: a compact, high-field, fusion nuclear science facility and demonstration power plant with demountable magnets, *Fusion Eng. Des.* **100** 378 (2015). doi:10.1016/j.fusengdes.2015.07.008

3 M E Austin *et al*, Achievement of reactor-relevant performance in negative triangularity shape in the DIII-D tokamak, *Phys. Rev. Lett.* **122** 115001 (2019). doi:10.1103/PhysRevLett.122.115001

4 A Marinoni, O Sauter and S Coda, A brief history of negative triangularity tokamak plasmas, *Rev. Mod. Plasma Phys.* **5** 6 (2021). doi:10.1007/s41614-021-00054-0

5 L L Lao, H St John, R D Stambaugh, A G Kellman and W Pfeiffer, Reconstruction of current profile parameters and plasma shapes in tokamaks, *Nucl. Fusion* **25** 1611 (1985). doi:10.1088/0029-5515/25/11/007

6 A Pironti and M Walker, Fusion, tokamaks, and plasma control: an introduction and tutorial, *IEEE Control Syst. Mag.* **25**(5) 30 (2005). doi:10.1109/MCS.2005.1512794

7 M Ariola and A Pironti, *Magnetic Control of Tokamak Plasmas*, 2nd edn (Springer, Cham, 2016).

8 F Felici *et al*, Real-time physics-model-based simulation of the current density profile in tokamak plasmas, *Nucl. Fusion* **51** 083052 (2011). doi:10.1088/0029-5515/51/8/083052

9 D Moreau *et al*, Integrated magnetic and kinetic control of advanced tokamak plasmas on DIII-D based on data-driven models, *Nucl. Fusion* **53** 063020 (2013).

10 J Degrave *et al*, Magnetic control of tokamak plasmas through deep reinforcement learning, *Nature* **602** 414 (2022). doi:10.1038/s41586-021-04301-9

11 J Seo *et al*, Avoiding fusion plasma tearing instability with deep reinforcement learning, *Nature* **626** 746 (2024).

12 J Kates-Harbeck, A Svyatkovskiy and W Tang, Predicting disruptive instabilities in controlled fusion plasmas through deep learning, *Nature* **568** 526 (2019). doi:10.1038/s41586-019-1116-4

13 A D Ames, X Xu, J W Grizzle and P Tabuada, Control barrier function based quadratic programs for safety critical systems, *IEEE Trans. Autom. Control* **62**(8) 3861 (2017).

14 A D Ames, S Coogan, M Egerstedt, G Notomista, K Sreenath and P Tabuada, Control barrier functions: theory and applications, *Proc. 18th European Control Conf. (ECC)* 3420 (2019).

15 D Q Mayne, J B Rawlings, C V Rao and P O M Scokaert, Constrained model predictive control: stability and optimality, *Automatica* **36**(6) 789 (2000).

16 E Garone, S Di Cairano and I Kolmanovsky, Reference and command governors for systems with constraints: a survey on theory and applications, *Automatica* **75** 306 (2017).

17 F Troyon, R Gruber, H Saurenmann, S Semenzato and S Succi, MHD-limits to plasma confinement, *Plasma Phys. Control. Fusion* **26**(1A) 209 (1984). doi:10.1088/0741-3335/26/1A/319

18 O Sauter, C Angioni and Y R Lin-Liu, Neoclassical conductivity and bootstrap current formulas for general axisymmetric equilibria and arbitrary collisionality regime, *Phys. Plasmas* **6** 2834 (1999). doi:10.1063/1.873240

19 G M Staebler, J E Kinsey and R E Waltz, A theory-based transport model with comprehensive physics, *Phys. Plasmas* **14** 055909 (2007).

20 J Candy, C Holland, R E Waltz, M R Fahey and E Belli, Tokamak profile prediction using direct gyrokinetic and neoclassical simulation, *Phys. Plasmas* **16** 060704 (2009).

21 J Candy, E A Belli and R V Bravenec, A high-accuracy Eulerian gyrokinetic solver for collisional plasmas, *J. Comput. Phys.* **324** 73 (2016). doi:10.1016/j.jcp.2016.07.039

22 J Candy and R E Waltz, An Eulerian gyrokinetic-Maxwell solver, *J. Comput. Phys.* **186** 545 (2003). doi:10.1016/S0021-9991(03)00079-2

23 C R Sovinec *et al*, Nonlinear magnetohydrodynamics simulation using high-order finite elements, *J. Comput. Phys.* **195** 355 (2004). doi:10.1016/j.jcp.2003.08.010

24 N C Amorisco *et al*, FreeGSNKE: a Python-based dynamic free-boundary toroidal plasma equilibrium solver, *Phys. Plasmas* **31** 042517 (2024). doi:10.1063/5.0188467

25 F Felici *et al*, Real-time-capable prediction of temperature and density profiles in a tokamak using RAPTOR and a first-principle-based transport model, *Nucl. Fusion* **58** 096006 (2018).

26 D Q Mayne, Model predictive control: recent developments and future promise, *Automatica* **50**(12) 2967 (2014).

27 L Lu, P Jin, G Pang, Z Zhang and G E Karniadakis, Learning nonlinear operators via DeepONet based on the universal approximation theorem of operators, *Nat. Mach. Intell.* **3** 218 (2021). doi:10.1038/s42256-021-00302-5

28 Z Li *et al*, Fourier neural operator for parametric partial differential equations, *Int. Conf. on Learning Representations (ICLR)* (2021). arXiv:2010.08895

29 M Raissi, P Perdikaris and G E Karniadakis, Physics-informed neural networks: a deep learning framework for solving forward and inverse problems involving nonlinear partial differential equations, *J. Comput. Phys.* **378** 686 (2019). doi:10.1016/j.jcp.2018.10.045

30 K L van de Plassche, J Citrin, C Bourdelle *et al*, Fast modeling of turbulent transport in fusion plasmas using neural networks, *Phys. Plasmas* **27** 022310 (2020). doi:10.1063/1.5134126

31 O Meneghini *et al*, Integrated modeling applications for tokamak experiments with OMFIT, *Nucl. Fusion* **55** 083008 (2015). doi:10.1088/0029-5515/55/8/083008

32 A J Creely *et al*, Overview of the SPARC tokamak, *J. Plasma Phys.* **86** 865860502 (2020). doi:10.1017/S0022377820001257

33 P I Ford, Negative-triangularity turbulence suppression in a compact spherical-tokamak breeder, Kronos Fusion Energy 2026 series. doi:10.5281/zenodo.22645722. kronosfusionenergy.com/publications/negative-triangularity-confinement.html

34 P I Ford, Free-boundary equilibrium and ideal-MHD stability of a compact spherical-tokamak breeder, Kronos Fusion Energy 2026 series. doi:10.5281/zenodo.22645740. kronosfusionenergy.com/publications/ideal-mhd-stability.html

35 P I Ford, Vertical stability at high elongation: displacement growth rates, control-coil authority, and VDE avoidance, Kronos Fusion Energy 2026 series. doi:10.5281/zenodo.22645834. kronosfusionenergy.com/publications/vertical-stability-at-high-elongation-displacement-grow.html

36 P I Ford, Bootstrap-aligned steady-state current sustainment without a central solenoid, Kronos Fusion Energy 2026 series. doi:10.5281/zenodo.22645758. kronosfusionenergy.com/publications/current-drive-and-bootstrap.html

37 P I Ford, From breakdown to flat-top: solenoid-free startup and disruption-free ramp access, Kronos Fusion Energy 2026 series. doi:10.5281/zenodo.22645760. kronosfusionenergy.com/publications/solenoid-free-startup.html

38 P I Ford, Poloidal-field coil set and equilibrium-current optimization for a compact spherical-tokamak breeder, Kronos Fusion Energy 2026 series. doi:10.5281/zenodo.22645945. kronosfusionenergy.com/publications/poloidal-field-coil-set-and-equilibrium-current-optimiz.html

39 P I Ford, A certified control-barrier safety filter for fusion control: forward-invariance guarantees, calibrated uncertainty, and an honest PINN negative, Kronos Fusion Energy 2026 series. doi:10.5281/zenodo.22645716. kronosfusionenergy.com/publications/control-barrier-safety-clamp.html

40 P I Ford, Maturity-gated actuation authority: binding PCMM verification credibility to runtime control authority, Kronos Fusion Energy 2026 series. doi:10.5281/zenodo.22645795. kronosfusionenergy.com/publications/maturity-gated-actuation-authority.html

41 P I Ford, Four coupled digital twins for a compact spherical-tokamak breeder: multi-rate co-simulation, propagated uncertainty, and a real-time self-consistency monitor, Kronos Fusion Energy 2026 series. doi:10.5281/zenodo.22645805. kronosfusionenergy.com/publications/four-coupled-digital-twins-for-a-compact-spherical-toka.html

42 P I Ford, A real-time optimization backbone for fusion plasma control: quadratic-programming, reduced-basis and adjoint-sensitivity engines at control latency, Kronos Fusion Energy 2026 series. doi:10.5281/zenodo.22645899. kronosfusionenergy.com/publications/a-real-time-optimization-backbone-for-fusion-plasma-con.html

43 P I Ford, AI and quantum computing for fusion: ML surrogates, real-time control, and a resource-honest quantum frontier, Kronos Fusion Energy 2026 series. doi:10.5281/zenodo.22645702. kronosfusionenergy.com/publications/ai-quantum-control.html

44 P I Ford, *Kronos Physics De-Risking Register*, Kronos Fusion Energy 2026 series. doi:10.5281/zenodo.22133057

COLOPHON

How this document was made

The Kronos Fleet — Combined Editorial, 2026 is set in **Fraunces** (display), **Gelasio** (text), and **IBM Plex Mono** (data & equations), carried forward from the Kronos editorial design system.

The figures are rendered at 300 dpi from the deposited generator scripts; the document is composed as a single self-contained file with embedded fonts and imagery, paginated to US Letter, and rendered to PDF through a headless Chromium engine in matched light and dark editions.

Every headline quantity carries an evidence class; withdrawn and restated values are marked as such. Nothing herein is frozen beyond the founder-approved Tier-A set.

Explore it live — turn the interactive 3-D model, run the deposited solvers in the physics validator, and watch the companion film series.

LEGAL NOTICE

Notice, status, and distribution

Conceptual design & simulation study. This document reports a conceptual design and simulation study. It is not a construction commitment, a safety-analysis report, a regulatory filing, or an offer of securities. Forward-looking statements — schedules, costs, market sizes, and performance — are estimates subject to the limitations set out in the Simulations part and may change.

Numbers and their classes. Quantities are reported with evidence classes and case labels; modelled, assumed, and requirement-class values are identified as such and are not to be quoted without their labels.

Public edition. This edition carries the physics and design only; all financial, funding, and defense-commercial content has been removed for public distribution. The scientific text corresponds to the arXiv and journal submissions.

THE 2026 KRONOS SERIES

One programme, many papers

This editorial is one paper in the Kronos 2026 series — a real fusion company's complete, reproducible physics record for a spherical-tokamak breeder and its low-neutron D–^{3}He tandem-mirror burners. Every headline number is a frozen anchor in the Physics De-Risking Register.

Explore the whole programme: the De-Risking Register, the interactive 3-D model, and the physics validator.

KRONOS FUSION ENERGY

A Real-Time Control Suite for a Compact Negative-Triangularity Spherical-Tokamak Breeder: Profile, Shape, Vertical-Stability, q-Profile, and Solenoid-Free Ramp Controllers

A real fusion company building real machines. Explore the science, live.

Zenodo · doi:10.5281/zenodo.22645809

Read on kronosfusionenergy.com

The Physics De-Risking Register